

# Far-Ultraviolet Imaging of the Hubble Deep Field North<sup>1</sup>: Star Formation in Normal Galaxies at $z < 1$

H. I. Teplitz<sup>2</sup>, B. Siana<sup>2</sup>, T. M. Brown<sup>3</sup>, R. Chary<sup>2</sup>, J. W. Colbert<sup>2</sup>, C. Conselice<sup>4</sup>, D. F. de Mello<sup>5,6,7</sup>, M. Dickinson<sup>8</sup>, H. C. Ferguson<sup>3</sup>, Jonathan P. Gardner<sup>5</sup>, F. Menanteau<sup>7</sup>

## ABSTRACT

We present far-ultraviolet (FUV) imaging of the Hubble Deep Field North (HDF-N) taken with the Solar Blind Channel of the Advanced Camera for Surveys (ACS/SBC) and the FUV MAMA detector of the Space Telescope Imaging Spectrograph (STIS) onboard the *Hubble Space Telescope*. The full WFPC2 deep field has been observed at 1600 Angstroms. We detect 134 galaxies and one star down to a limit of  $FUV_{AB} \sim 29$ . All sources have counterparts in the WFPC2 image. Redshifts (spectroscopic or photometric) for the detected sources are in the range  $0 < z < 1$ . We find that the FUV galaxy number counts are higher than those reported by GALEX, which we attribute at least in part to cosmic variance in the small HDF-N field of view. Six of the 13 *Chandra* sources at  $z < 0.85$  in the HDF-N are detected in the FUV, and those are consistent with starbursts rather than AGN. Cross-correlating with *Spitzer* sources in the field, we find that the FUV detections show general agreement with the expected  $L_{IR}/L_{UV}$  vs.  $\beta$  relationship. We infer star formation rates (SFRs), corrected for extinction using

---

<sup>1</sup>Based on observations made with the NASA/ESA *Hubble Space Telescope*, obtained from the Space Telescope Science Institute, which is operated by the Association of Universities for Research in Astronomy, Inc., under NASA contract NAS 5-26555. These observations are associated with proposals 7410 and 9478.

<sup>2</sup>Spitzer Science Center, MS 220-6, Caltech, Pasadena, CA 91125. hit@ipac.caltech.edu

<sup>3</sup>Space Telescope Science Institute, 3700 San Martin Drive, Baltimore, MD 21218

<sup>4</sup>University of Nottingham, Nottingham, NG7 2RD, UK

<sup>5</sup>Exploration of the Universe Division, Observational Cosmology Laboratory, Code 665, Goddard Space Flight Center, Code 681, Greenbelt, MD 20771

<sup>6</sup>Department of Physics, Catholic University of America, 620 Michigan Avenue, Washington, DC 20064

<sup>7</sup>Department of Physics and Astronomy, Johns Hopkins University, 3400 North Charles Street, Baltimore, MD 21218

<sup>8</sup>NOAO, 950 N. Cherry Ave., Tucson AZ 85719

the UV slope, and find a median value of  $0.3 \text{ M}_{\odot}/\text{yr}$  for FUV-detected galaxies, with 75% of detected sources have  $\text{SFR} < 1 \text{ M}_{\odot}/\text{yr}$ . Examining the morphological distribution of sources, we find that about half of all FUV-detected sources are identified as spiral galaxies. Half of morphologically-selected spheroids at  $z < 0.85$  are detected in the FUV, suggesting that such sources have significant ongoing star-formation in the epoch since  $z \sim 1$ .

*Subject headings:* cosmology: observations — galaxies: evolution — ultraviolet: galaxies

## 1. Introduction

The star formation rate density of the Universe, integrated over all galaxy populations, shows a sharp decline since redshifts near unity (e.g., Madau et al. 1996, 1998). While the precise shape of the decline with redshift is still uncertain (Lilly et al. 1996; Hogg et al. 1998; Flores et al. 1999; Wilson et al. 2002), its existence points to a “downsizing” in galaxies that host most of the star formation at  $z < 1$  (Cowie et al. 1996). The characteristics (morphology, mass, luminosity) of these low redshift starbursts may explain the global decline in star formation. Wolf et al. (2005) suggest that the decline is dominated by decreasing star formation in normal spiral galaxies rather than, for example, the decreasing rate of major mergers.

Ultraviolet (UV) emission is an indication of recent star formation in a galaxy. Despite absorption by dust, the rest-frame UV is strong enough in the majority of star-forming galaxies to be detected in current surveys (Adelberger & Steidel 2000). UV detection can distinguish star-forming from quiescent systems, and indicates the amount of recent star formation, subject to the effects of extinction by dust (e.g., Calzetti et al. 1994; Fitzpatrick 1986; Meurer et al. 1999; Buat et al. 2005). Far-ultraviolet (FUV) surveys, in particular, can provide direct evidence of recently formed, massive stars in the dominant populations at  $z < 1$  (Schiminovich et al. 2005).

Of particular interest is the the star-formation activity present in early type galaxies. Recent studies have shown that some galaxies which appear morphologically to be spheroids have, nonetheless, substantial ongoing star formation. Yi et al. (2005) find that at least 15% of bright, local ellipticals show evidence of recent star formation, ruling out pure monolithic collapse histories for at least that fraction of such sources. Similarly, studies of the internal color variations in elliptical galaxies have shown almost one third of them show gradients inconsistent with passive evolution (Abraham et al. 1999; Menanteau et al. 2001; Papovich

et al. 2003). The formation of spheroid galaxies, then, is a crucial component of successful hierarchical models. Conselice et al. (2005) find that the massive galaxies at  $z < 1$ , both spirals and ellipticals, likely have major-merger progenitors at higher redshifts. Nonetheless, a significant fraction of stellar mass must still have formed since  $z \sim 1$  (Bell et al. 2004; Dickinson et al. 2003). The assembly of that additional stellar mass should be detectable in UV surveys.

We present a far-ultraviolet (1600 Å; FUV) imaging survey of the Hubble Deep Field North (HDF-N; Williams et al. 1996). The data were taken in two surveys. The first utilized the FUV camera of the Space Telescope Imaging Spectrograph (STIS; Kimble et al. 1998; Woodgate et al. 1998) to survey a small part of the field. That portion of the data set has been used to measure galaxy number-magnitude counts (Gardner et al. 2000a) and the diffuse FUV background emission (Brown et al. 2000a). We surveyed the remaining area with the Solar Blind Channel (SBC) of the Advanced Camera for Surveys (Ford et al. 1998). We outline the survey and data reduction in Section 2 and present the catalog in Section 3. In Section 4, we discuss the properties of FUV-detected sources at other wavelengths, the inferred star formation rates, and the implications of the detection of elliptical galaxies. Throughout, we assume a  $\Lambda$ -dominated flat universe, with  $H_0 = 70$  km s<sup>-1</sup> Mpc<sup>-1</sup>,  $\Omega_\Lambda = 0.7$ ,  $\Omega_m = 0.3$ . Photometry is presented with magnitudes on the AB system which is defined by  $AB = -2.5 \log F_\nu - 48.6$ , where  $F_\nu$  is given in units of ergs cm<sup>-2</sup> s<sup>-1</sup> Hz<sup>-1</sup> (Oke 1971).

## 2. Observations and Data Reduction

FUV imaging of the HDF-N was obtained in two HST General Observer programs (No. 7410 with STIS and No. 9478 with ACS/SBC). The ACS survey is composed of fourteen 2-orbit pointings covering 3.77 square arcminutes. Each pointing consisted of 16×640 seconds exposures with dithers of  $\sim 10$  pixels. The field of view of the ACS/SBC detector is 34.6''×30.8''. The images were obtained with the long pass quartz filter (F150LP) with an effective wavelength of 1614 Å and  $FWHM = 177$  Å. The STIS survey covered 1.02 square arcminutes in six pointings for a combined exposure time of 124,330 seconds. The field of view of the STIS detector is 25''×25''. The images were obtained through the crystal quartz filter (F25QTZ) with a central wavelength of 1595 Å and  $FWHM = 193$  Å.

Both the STIS and ACS/SBC filters are long-pass filters with a short wavelength cutoff at  $\lambda < 1480$  Å. The STIS and ACS/SBC detectors are both Multi-Anode Microchannel Arrays (MAMAs) and have similar spectral response curves which fall off slowly from 1500 to 1800 Å. Therefore, the combined filter+detector system response curves of the STIS and

ACS/SBC FUV configurations is similar, with the only significant difference being that the ACS/SBC throughput is non-zero at  $1850 \text{ \AA} < \lambda < 2000 \text{ \AA}$  (Figure 1).

Data for both surveys were reduced following the procedure outlined in Gardner et al. (2000b). Full details of the STIS data reduction are given in that paper, and ACS-specific reductions are discussed here.

The MAMA detector has no read noise and is insensitive to cosmic rays. The primary source of noise is dark current, which has two components. When the temperature of the MAMA is below 20C, the dark current is fairly uniform with an average count rate of  $\sim 8 \times 10^{-6} \text{ counts s}^{-1} \text{ pixel}^{-1}$ . However, as the SBC is being used, the MAMA warms up and produces an additional temperature-dependent dark “glow” near the center of the detector. Therefore, we subtract the dark current in two stages. First we subtract the primary calibration dark which was made from darks collected at  $T < 20\text{C}$ . We then make a residual dark by summing up all of the initial dark subtracted frames and fitting a two dimensional, fifth-order spline curve. The isophotal segmentation maps from the HDF-North Wide-Field Planetary Camera 2 (WFPC2) V+I images (Williams et al. 1996) were used to mask areas contaminated by known objects using the *blot* capability of the DRIZZLE package in IRAF. We then subtracted the residual dark after scaling to the average of a region near the peak of the dark “glow”. We find that  $< 2\%$  of the secondary dark remains after this second subtraction.

The dark rate of the secondary “glow” near the center of the chip is typically larger than that of the initial (i.e., at  $T < 20\text{C}$ ) dark rate and is a function of the temperature of the MAMA tube. The MAMA tube gets warmer as the SBC is used, and we find that the count rate increases linearly with time with the rate near the center of the chip increasing by  $\sim 2.5 \times 10^{-5} \text{ counts}^{-1} \text{ s}^{-1} \text{ pixel}^{-1} \text{ hour}^{-1}$  (see Figure 2). Equivalently, this amounts to increasing the dark rate by an amount equal to the “cold” dark rate every 20 minutes. Some of our scheduled visits were longer than 6 hours with entire pointings done at the end of the visit. Therefore the dark rate for these pointings was a factor of 10-20 times larger than in those taken at the beginning of a visit, resulting in a decrease in sensitivity of  $\sim 1\text{-}2$  magnitudes in the “glow” regions. Therefore, large SBC programs in the future would greatly benefit from segmenting their observations into multiple visits.

Standard calibration files were used for flat fielding, geometric distortion correction and photometric calibration. Individual reduced images were registered and summed using the DRIZZLE package in IRAF<sup>1</sup>. Both ACS and STIS data were drizzled to the pixel scale of the HDF-N WFPC2 data products ( $0.03985'' \text{ pixel}^{-1}$ ), and matched to the WFPC2 pixel

---

<sup>1</sup>IRAF is distributed by NOAO, which is operated by AURA Inc., under contract to the NSF

positions. Shifts between the 16 dithered positions of each pointing were assumed to be exactly as commanded. This assumption is reasonable, given the small-offset accuracy of HST (3-5 mas). The registration of the 14 pointings was done by matching the FUV sources to the  $B_{450}$  WFPC2 image and computing shifts, rotation, and scaling with the GEOMAP routine in IRAF. For all 14 pointings, the rms fit was  $< 0.03''$ .

As discussed by Gardner et al. (2000b) and Brown et al. (2000a), the dark current is the principle source of noise in MAMA imaging. The individual frames were weighted by the square of the exposure time, divided by the total dark (initial + secondary). As the dark count scales with exposure time, these weight maps scale linearly with the ratio of exposure time to dark rate. Therefore, the final weight maps are the square of the signal-to-noise ratio for objects fainter than the background.

Photometry was performed by summing the pixel values within the source areas defined by the  $3.25\sigma$  isophotes (where  $\sigma$  is the rms background noise) in the V+I WFPC2 segmentation map produced by SExtractor (Bertin & Arnouts 1996). The V+I image was used because it is the most sensitive image, and therefore the  $3.25\sigma$  isophotes are contiguous (i.e. individual galaxies are not broken into several isophotes) and encompass the large majority of the galactic light for all but the faintest galaxies. To validate this method we extracted fluxes in the  $B_{450}$  image with  $3.25\sigma$  and  $0.65\sigma$  V+I isophotes. The fluxes derived with the smaller  $3.25\sigma$  isophotes missed 10–15% of the flux within the larger  $0.65\sigma$  isophote, but were significantly less noisy. We therefore use the smaller isophotes for detection and the ratio of the two fluxes (in the F450W image) as an aperture correction. Again, we verified that these “aperture corrected” UV fluxes agreed well with the fluxes derived in the larger aperture, but with smaller errors. For the few objects with aperture corrections larger than 40%, the larger apertures were used.

### 3. Results

Figure 3 shows the fully reduced, registered FUV mosaic. We detect 128 sources above a signal-to-noise ratio,  $\text{SNR} > 3.5$ . We add an additional 7 sources by hand because their UV flux is more compact and the larger V+I segmentation map causes large errors in the flux estimates. The FUV properties of the 135 sources are given in Table 1. The detection limits vary significantly between pointings due to large variations in dark “glow”. In those regions least affected by the dark “glow”, the  $3.5\sigma$  limiting magnitudes are  $FUV_{AB} = 29.2$  in the STIS survey and  $FUV_{AB} = 28.8$  in the ACS Survey for a  $1''$  diameter aperture.

Published spectroscopic redshifts are available for 60 of the 135 FUV detected sources

(Cohen et al. 2000; Cohen 2001; Dawson et al. 2001). One spectrum shows the object to be a star. For the remaining objects, photometric redshifts have been estimated based on WFPC2  $U_{300}B_{450}V_{606}I_{814}$ , NICMOS  $J_{110}H_{160}$ , and ground-based  $Ks$  (Budavári et al. 2000). There were 12 objects that did not have NICMOS identifications because they were either too faint or were incorrectly associated with other galaxies/stars. Two objects have published photometric redshifts at  $z > 1$ , which would place the FUV filter blueward of the 912Å break. One object has  $z_{phot} = 1.09$  so can easily be at  $z < 1$ . The second source is at  $z_{phot} = 2.18$  but appears to be coincident with a background object with different optical colors. Figure 4 show the distribution of redshifts.

In the following analyses, we have removed 10 of the 135 sources for various reasons: the object lies on the edge of the UV image (4 sources), the object lies on the edge of the NICMOS image (1 source), either the NICMOS or WFPC2 apertures encompass more than one source and therefore have compromised photometric redshifts (3 sources), or the object is a star (1). We also exclude an elliptical at  $z = 0.089$  from analysis involving FUV to optical colors, because the FUV light is centered on a very small region compared to the very large aperture containing the light in the F300W and other filters; this difference, combined with the low redshift will result in the F300W being dominated by light from older stars at the red end of the filter. These objects and their fluxes are included in 1 with footnotes denoting the object specific problem.

## 4. Discussion

### 4.1. Number Counts

We measure galaxy number-magnitudes for the ACS sources and compare them to the published STIS counts (Figure 5). Dark current variation complicates the measurement of the counts. We use the procedure outlined in Gardner et al. (2000a). First, we use the variance map to determine the area over which each galaxy would have been detected. The STIS and ACS counts are generally consistent. Only one object was measured in common.

In the figure, we also compare the HST number counts to the FUV number counts measured by GALEX (Xu et al. 2005), XMM (Sasseen et al. 2002), and FOCA (Milliard et al. 1992). These other counts reach measurement reached  $FUV_{AB} \leq 24$ . We correct the XMM and FOCA counts from their central wavelength of 2000 Å to 1500 Å following Xu et al. by assuming a UV slope,  $\beta = -0.8$ . We do not include a color correction for the difference between the ACS and GALEX filters, but we estimate that such a correction could be substantial for distant sources (see Figure 6). The difference for  $z > 0.5$  is the result of

the bluer wavelength coverage of the GALEX filter, which is more strongly affected by the 912 Å limit (see Figure 1). The redshifting of the Lyman limit combined with the redder transmission of the ACS filter causes it to be sensitive to a larger volume than the GALEX filter, by a factor of  $\sim 30\%$ . For  $z \sim 0.15$  sources, the color correction is reversed for sources with strong Ly $\alpha$  emission lines falling in the GALEX filter but below the blue end of the F150LP filter. About half of the ACS sources lie at  $z > 0.5$ . The color correction would be less extreme for the STIS filter, which had a red-end cutoff between that of GALEX and ACS.

The HST counts are higher (by a factor of  $\sim 2$ ) than both the GALEX counts and the model which fits them. At  $FUV_{AB} \leq 24$ , the discrepancy is only marginally significant as the ACS counts lie within 1-2  $\sigma$  of the the GALEX counts. The XMM and FOCA counts are also higher than GALEX at these magnitudes. The difference with the model is more significant, as it is repeated over a larger number of bins.

The GALEX counts are fit by a model which assumes essentially pure luminosity evolution,  $L_* \sim (1+z)^{2.5}$ , and a starburst SED that is flat between 1000 and 1200 Å (Xu et al. 2005). The HST counts are significantly higher than the model. Some of this difference is the result of the filter difference discussed above, which causes a  $\sim 30\%$  difference in the volume surveyed and potentially a half magnitude of color-correction. Thus, there cannot be much more than a factor of  $\sim 2$  between the counts and the model. The most likely explanation for this difference is cosmic variance. The HST counts are dominated by the very small field of view of the HDF-N, as the STIS counts include only a single pointing in the HDF-S and seven in the HDF-N. The northern sightline is known to have source overdensities at  $z \sim 0.45$  and  $z \sim 0.8$  (Cohen et al. 2000). So, it may not be surprising that the HST counts are higher. Somerville et al. (2004) estimate that in a typical area the size of the HDF, the cosmic variance of highly clustered sources is a factor of  $\sim 2$ . We also note that the higher HST counts could indicate that the pure luminosity evolution model is not sufficient at the faintest UV fluxes, and perhaps number density evolution is required as well.

Gardner et al. (2000a) report that the FUV number counts measured from the STIS subset of the data are surprisingly flat compared to the predicted counts (Granato et al. 2000). We see no significant change in the slope with the addition of the ACS data.

Finally, we also examined the HST data to determine whether the difference in spatial resolution between GALEX and HST could result in source confusion. There is no evidence of confusion in the HDF at the depth of the Xu et al. (2005) counts,  $FUV_{AB} < 24$ . However, at the depth of the GALEX ultra-deep surveys,  $FUV_{AB} \sim 26$ , some individual sources would be confused. The 34 sources brighter than 26 in the ACS area would correspond to  $\sim 20$  beams per source at the GALEX resolution.

## 4.2. Star Formation Rates and Comparison to Other Wavelengths

The detection of HDF-N sources in the FUV provides a sample of starbursts, and other star-forming galaxies, out to redshifts near unity. We can compare their FUV properties to the extensive data available in the field outside of the HST wavelength range.

Strong starbursts should also be mid-infrared (MIR) bright galaxies. UV light absorbed by dust is re-radiated in the far-IR; and heated dust grains themselves, both small grains and polycyclic aromatic hydrocarbons (PAHs), emit in the mid-IR. The “Great Observatories Origins Deep Survey” (GOODS; Dickinson et al. 2005, in prep.) Spitzer Legacy Program has obtained ultra-deep observations of the field with the Infrared Array Camera (IRAC; Fazio et al. 2004) and the 24  $\mu\text{m}$  array of the far-IR photometer (MIPS Rieke et al. 2004). Only 56 of the FUV sources are detected by IRAC and 18 by MIPS at  $\geq 2\sigma$ . For comparison, we examine the IRAC catalog for the *Chandra* Deep Field South (Dickinson et al. 2006, in preparation) with the publically available GALEX catalog<sup>2</sup>. We find that the average FUV-IRAC1 color is 2.1 magnitudes. The HDF FUV image reaches  $AB \geq 29$  while the IRAC channel 1 image reaches  $AB \sim 25$  (completeness limit due to confusion), so UV-luminous objects with typical colors will be more easily detected in the FUV.

The MIR luminosity of local galaxies in the IRAS bright galaxy sample (Soifer et al. 1987) has been found to correlate strongly with their far-infrared luminosity which is dominated by large, cool dust grains (Chary & Elbaz 2001). This correlation has been applied to develop a library of model templates of the mid- and far-infrared SED of galaxies. The library consists of template SEDs across a range of luminosities, which can be redshifted to predict the MIR flux of a source with given luminosity at a redshift of interest. For each source in the FUV sample, we select the template for which the library predicts the closest 24  $\mu\text{m}$  flux density at the appropriate redshift to apply a bolometric correction; we do not use the shorter wavelength IRAC measurements. The corrections based on the Chary & Elbaz (2001) and Dale & Helou (2002) template are used to derive an infrared luminosity ( $L_{IR} = 8 - 1000 \mu\text{m}$ ). This technique of deriving the bolometric luminosity from the rest-frame MIR luminosity is shown to be accurate to 40% in the local Universe (Chary & Elbaz 2001). The difference between the derived  $L_{IR}$  from the two templates is assumed to be representative of the systematic uncertainty in the bolometric correction. Statistical uncertainties are assumed to correspond to the signal to noise ratio of the source at 24  $\mu\text{m}$ . The validity of the mid- to far-infrared correlation and the one-to-one correlation between the bolometric correction and the MIR luminosity has been tested for field galaxy samples out to  $z \sim 1$  (Appleton et al. 2004; Marcillac et al. 2005). The MIPS detected sources have

---

<sup>2</sup><http://galex.stsci.edu/GR1>



a median luminosity of  $\sim 10^{10} L_{\odot}$  with four sources falling in the class of luminous infrared galaxies (LIRGs;  $L_{IR} \gtrsim 10^{11} L_{\odot}$ ). Figure 7 shows the inferred luminosity of FUV sources detected by MIPS.

Meurer et al. (1999) find a correlation between the the UV slope  $\beta$  and ratio of infrared luminosity to UV luminosity for starburst galaxies, where  $f_{\lambda} \propto \lambda^{\beta}$ . We measure this slope by combining the FUV data with WFPC2 photometry in order to measure the slope of the UV continuum from the available data. We estimate the value of  $\beta$  following the technique used by Meurer et al. (1999). We begin with 17 spectra from the catalog of Kinney et al. (1993), spanning a range in  $\beta$  as measured by Meurer et al. After “redshifting” each spectrum from  $z = 0$  to  $z = 0.85$  in steps of  $\delta z = 0.1$ , we integrate under the filter transmission curves for the ACS F150LP, and the WFPC2 F300W and F450W at each redshift. For each redshift, this allows us to define a linear relation between the color of the object and its intrinsic FUV slope, yielding a function for  $\beta(z, \text{color})$ . At low redshift we use the F150LP-F300W color. At  $z > 0.4$ , the F150LP filter contains little information redward of restframe 1000 Å, so we use the F300W–F450W color. We estimate the error in  $\beta$  to be  $\sim 30\%$  from the photometric uncertainty combined with the formal error in the linear fit to the template values. In the redshift range  $0.2 < z < 0.4$  the F150LP filter includes the Ly $\alpha$  line, which can strongly affect the estimate of  $\beta$ ; furthermore, at these redshifts the FUV filter is strongly affected by the flattening of the  $< 1200$  Å continuum Buat et al. (2002). Thus, we will consider values for objects at that redshift to be 50% more uncertain; there are only 6 objects with IRAC counterparts in that range.

We obtain  $\beta$  values with a median of  $-1.2 \pm 0.6$ , with no clear trend in redshift or FUV magnitude. Schiminovich et al. (2005) measure the UV slope for nearly one thousand galaxies out to  $z \sim 1$  with  $FUV_{AB} < 24$ , using GALEX photometry and VVDS redshifts. They report a median slope  $\beta_{GLX} = -1.44 \pm 1$  for sources where confusion is not an issue, in good agreement with other estimates (Treyer et al. 2005; Adelberger & Steidel 2000).

For each source, we also estimate the FUV luminosity ( $\nu L_{\nu}$ ) at rest-frame 1600 Å, using the derived value of  $\beta$  and the flux density in either F150LP or F300W, whichever is closer in the rest frame. In Figure 8, we plot the ratio of inferred  $L_{IR}$  to  $L_{FUV}$  (hereafter  $IRX$ ) against the slope of the UV continuum and indicate the inferred  $L_{IR}$  of the sources. We find that the relationship of Meurer et al. (1999) is generally reproduced for the more luminous objects. Less luminous sources tend to fall below the line, a trend already noted in GALEX results by Seibert et al. (2005). In the figure, we also plot the  $\beta$  relationship measured by Cortese et al. (2005) for normal star-forming galaxies which are less luminous than the Kinney et al. starbursts. The less luminous objects in our sample approximately follow the normal galaxy relation. Alternately, these sources may have a contribution from older stars

to the filters used in the fit, causing their  $\beta$  values to appear redder. This latter explanation may be less likely, as our sample is FUV-selected, while the Coresse et al. sample is not. Burgarella et al. (2005) find that the influence of older stars to the UV colors of galaxies in a UV-selected sample is small. At the other extreme, infrared luminous sources have been observed to generally have higher  $IRX$  for a given  $\beta$  than the starburst galaxies in the Meurer et al. sample (Goldader et al. 2002). The brightest LIRG in our sample does lie slightly above the line.

#### 4.2.1. Star Formation Rates

FUV imaging provides a powerful tool for measuring the star formation in normal galaxies, but is strongly affected by extinction. We can derive the star formation rate (SFR) for each galaxy from the detected FUV flux. Kennicutt (1998) gives the calibration from the 1500 Å continuum to the SFR:

$$\text{SFR}(\text{M}_{\odot} \text{ yr}^{-1}) = 1.4 \times 10^{-28} L_{\text{FUV}} (\text{ergs s}^{-1} \text{Hz}^{-1}),$$

assuming a Salpeter IMF (Salpeter 1955) with mass limits of 0.1-100  $\text{M}_{\odot}$  and continuous star formation. The Meurer et al. (1999)  $IRX$  relation suggests a calibration for the dereddening factor of  $A_{\text{FUV}} = 4.43 + 1.99(\beta)$ , expressed in magnitudes. For the FUV-detected sources, we obtain a median extinction factor, as a multiple rather than in magnitudes, of  $\sim 6$ . The relationship assumes, however, that the UV flux is entirely the product of young stars. Our sample likely includes sources with only moderate star formation, ordinary spirals and even elliptical galaxies, so the flux within the filter wavelength range (particularly in the WFPC2 filters) may include some contribution from an older (or aging) stellar population. The star formation rates (SFRs) that we infer will thus be upper limits. In Figure 9, we show the inferred star formation rates for FUV sources as a function of redshift and morphology.

#### 4.2.2. X-ray Properties

The Chandra 2 Ms catalog (Alexander et al. 2003) contains 13 sources within the FUV survey area with spectroscopic redshifts of  $z < 0.85$  from the catalog of Barger et al. (2003). Six optical counterparts to these X-ray sources are detected in the FUV. These objects lie at redshifts 0.089, 0.139, 0.475, 0.556, and 0.752. The object at 0.321 is described by Barger et al. (2003) as a possible multiple structure contaminated by a foreground object; the optical/FUV counterpart is more than an arcsecond from the X-ray position. Three of

the FUV counterparts are spatially extended, and the other three are extremely faint in the FUV but extended in the F450W filter. None of them are detected in the hard band, none have broad optical emission lines (Barger et al. 2003) and all are near the detection limit of the softband (0.5-2 keV), with fluxes  $SB \leq 0.08$  ergs cm<sup>-2</sup> s<sup>-1</sup>. These properties are consistent with the interpretation that the source of the X-rays is star formation rather than active galactic nuclei. Similarly, the Ranalli et al. (2003) calibration of X-ray luminosity as a star formation indicator yields rates generally in agreement (within a factor of a few) with the UV-inferred SFR.

### 4.3. Morphological Distributions

FUV imaging picks out the location of the most recent star formation. Photometry tells us the total SFR; morphology tells us where it occurs within the galaxies. As a result, the appearance of a galaxy can vary dramatically in different passbands even in the absence of dust, (a “morphological k-correction”, see Papovich et al. 2003, and the references therein). In Figure 10, we compare the morphologies of selected UV-bright galaxies in the FUV. As expected, some galaxies appear similar across wavelengths while others show substantial differences. Truly irregular or morphologically disturbed galaxies tend to appear similar across wavelength, as do some elliptical galaxies (see counter examples in Windhorst et al. 2002). The morphological K-correction is most pronounced for early to mid-type spirals, in which a substantial population of old stars defines the optical shape, but regions of recent star formation are “lit up” across the galaxy (Windhorst et al. 2002).

We avoid the K-correction by matching the FUV detections to a morphological catalog of galaxy types (Conselice et al. 2005) and CAS parameters (see Conselice 2003). The catalog includes galaxy morphologies in the rest-frame B-band for the 200 HDF galaxies out to  $z = 0.85$  that are bright enough for visual classification (out of 240 possible). We restrict our analysis to  $z < 0.85$  because the redshifting Lyman break leaves little flux within the F150LP filter at higher redshift. We exclude 10 sources that are not in the Conselice et al. (2005) catalog, mostly due to the lack of NICMOS counterparts.

This gives us some indication of the types of galaxies that are emitting in the FUV at redshifts  $z < 1$ . We find that the galaxies detected in the FUV span all the major morphological types, as also seen by de Mello et al. (2004). Figure 11 shows the morphological break down for systems based on their apparent morphological types as classified by Conselice et al. (2005). As can be seen the spiral galaxies dominate the number counts for the FUV sources, although spheroids make up a significant fraction of the detections at  $z > 0.6$  and irregulars are also represented. We find, in fact, that a significant fraction of all spheroids

(30/56) and a similar fraction of spirals (50/87) at  $z < 0.85$  are detected in the FUV in the HDF-N.

The relative distributions of FUV emitting types with redshifts can be seen in Figure 12, which plots the absolute  $M_B$  magnitude as a function of redshift. From this diagram, there is a broad range of absolute magnitudes for the FUV sources at all redshifts. The median luminosity for UV-detected spheroids, spirals, and irregulars is  $-17.3$ ,  $-18.2$ , and  $-16.2$ , respectively, compared to median values of  $-17.7$ ,  $-17.8$ , and  $-16.4$  for all galaxies of the three types at  $z < 0.85$  in the HDF. Interestingly, while the median values agree, the most luminous ellipticals in the HDF ( $M_B < -19$ ) are not generally detected in the FUV (3 out of 11).

The figure shows that less than half of peculiar/irregular at  $z < 0.85$  are detected in the FUV; only 38% (18/47) have FUV detections. This is due in large part to their intrinsic faintness, rather than unusually red color. Half of the irregulars have V-band magnitudes fainter than 27, which makes them undetectable in some or all areas of the FUV image. The FUV-detected irregulars are somewhat bluer than the rest of the UV sample, with a median value of  $FUV_{AB} - V_{AB} \sim 1.3$  compared to a median color of 1.5 for the entire FUV catalog. These same objects are optically blue, with a median  $V - I \sim 0.5$  compared to 0.6 for the all  $z < 0.85$  sources in the HDF.

#### 4.4. Star formation in Spheroids

We find evidence for star formation in  $\sim 50\%$  of spheroids at  $z < 0.85$ . These objects are typically less massive than  $10^{10} M_\odot$  (see Figure 14) and less luminous than  $M_B = -19$ . Their sizes (half light radii) are similar to other spheroids in the HDF. We find a median SFR of  $0.25 M_\odot \text{ yr}^{-1}$ , after extinction correction (see Section 4.2).

So far, we have only considered morphologically-selected spheroids. However, few of these objects have the SED of purely old stellar populations, even without including the FUV. Stanford et al. (2004) show that morphologically- and spectroscopically-identified spheroids in the HDF are not necessarily the same population. A morphological selection identifies sources which have SEDs similar to local spheroids and identifies additional sources that are bluer, less massive, and less luminous than those. Only one of the objects in the Stanford et al. (2004) sample of spectroscopic ellipticals is detected in the FUV. Their sample of morphologically selected ellipticals is not identical to that of Conselice et al. (2005), but the fraction of FUV detections is similar. The FUV detection, then, supports the Stanford et al. (2004) conclusion that some morphological spheroids have recent or ongoing star formation.

This effect has also been seen in the “blue-core” ellipticals (Menanteau et al. 2001). These objects were initially identified by strong color gradients in the WFPC2 images, which show significant bluing towards the center. The presence of the blue cores suggested a population of young ( $< 1\text{Gyr}$ ) ellipticals which may have undergone recent merger activity or some type of residual star formation. Ten of the 21 sources at  $z < 0.85$  in the Menanteau et al. sample are detected in the FUV. In Figure 13, we show that the sources with the bluest cores are the ones most likely to be detected in the FUV. The detection of FUV flux near the core of the sources confirms that these objects have small amounts of ongoing star formation.

It is highly unlikely that the FUV flux detected in spheroids is the result of the “UV upturn” that arises from a minority population of hot horizontal branch stars (e.g. Brown et al. 1997). For example, cluster ellipticals at  $z = 0.33$  and  $z = 0.55$  have been observed to show small amounts of UV emission (Brown et al. 2000b, 2003). Unlike the HDF spheroids, these objects have optical SEDs broadly consistent with old stellar populations. The UV emission in UV-upturn galaxies is a small fraction of the total luminosity. Brown et al. (2003) find  $m_{1500} - V \sim 4$  for UV-upturn galaxies, while the median color of the HDF spheroids is  $\sim 2$  mag. and only one of them has a color greater than 3. The differences in the STIS and ACS filters could account for ACS objects being  $\sim 0.4$  magnitudes brighter than their STIS counterparts at  $z > 0.2$ , but the HDF spheroids are still significantly brighter in the UV. Similarly, Brown et al. (2003) estimate that the flux associated with the UV upturn would correspond to  $SFR \sim 0.005 - .02 \text{ M}_{\odot}/\text{yr}$  if it arose instead from star formation. The inferred SFR in HDF spheroids is a factor of several higher even without extinction correction, and significantly higher with the correction. However, we note that an old stellar contamination of the redder filters could result in an overestimate of the SFR. Thus it is likely, though not certain, that most of the UV flux in HDF spheroids is the result of star formation and not the UV upturn.

The more massive and luminous ellipticals in the HDF appear not to be forming stars at rates similar to the smaller and fainter ones that we detect in the FUV. This could be a direct indication that lower luminosity ellipticals in the field form later than the giant ellipticals. This is consistent with the widely varying ages measured for local ellipticals (Trager et al. 2000). Such a distinction may be evidence of downsizing in the galaxy formation process, which may be directly related to the rate of merging which is seen to be high for lower luminosity and lower mass galaxies at  $z < 1$  (Conselice et al. 2003).

Another way to investigate the star-formation nature of early type galaxies is by examining their location in the concentration-asymmetry diagram for galaxies at  $z < 1$  (Figure 15). The most evolved spheroids which have had no star formation in the recent past, should

contain a high concentration and a low asymmetry. These objects typically do not have FUV emission. On the other hand, morphologically-identifiable spheroids with high asymmetries, that indicate a recent evolution, are more likely than not to have FUV emission. This result supports the conclusion that the FUV emission is originating from star formation, which produces the structural asymmetries. Furthermore, many of the FUV-detected spheroids have relatively low concentrations, consistent with their morphology tracing the regions of young stars as well as the underlying older population (e.g. Windhorst et al. 2002).

The inferred SFR in HDF spheroids is not high enough for them to be the progenitors of local giant ellipticals, but it may suggest that a significant fraction of the stars in lower luminosity and lower mass ellipticals form at  $z < 1$ . There is no evidence that the FUV detected spheroids are undergoing the last years of a final episode of star formation. Instead, we might estimate a duty cycle of star formation episodes. The detection fraction ( $\sim 50\%$ ) suggests that these objects could spend as much as half the time producing small amounts of stars. With a median SFR of  $0.3 \text{ M}_\odot/\text{yr}$ , this duty cycle would allow as much as  $\sim 10^9 \text{ M}_\odot$  to form between  $z = 0.85$  and  $z = 0$ . The median stellar mass estimated by Conselice et al. (2005) for the spheroids is  $\sim 10^{8.5} \text{ M}_\odot$ , so they could double or triple in size by present day. They would still remain much less massive than the spectroscopically-identified ellipticals, which typically have stellar masses greater than  $10^{10} \text{ M}_\odot$  (Stanford et al. 2004).

## 5. Summary

We have obtained FUV imaging of the Hubble Deep Field North using the Solar Blind Channel (SBC) of the ACS and FUV MAMA of the STIS. We achieve  $3.5\sigma$  sensitivities fainter than  $FUV_{AB} \sim 29$ . We detect 134 galaxies and one star. We have compared our results to the multiwavelength data available for the field. We find the following:

1. The enhanced dark current “glow” in the center of the SBC chip is a strong function of detector temperature, which rises sharply during observation visits longer than two orbits. Future large SBC programs would benefit from breaking observations into multiple short visits.

2. Galaxy number-magnitude counts for the full survey generally agree with those previously published for a subset of the data, but are a factor of  $\sim 2$  higher than a model fit to counts measured by GALEX at the brighter magnitudes. We attribute the difference to a combination of: a) differences in the FUV filter transmission between the two observatories, and b) cosmic variation resulting from the small field of view of the HDF-N. We see no evidence for source confusion at the level of the current GALEX counts,  $FUV_{AB} \sim 24$ , but

find that confusion may be an issue in the ultra-deep GALEX survey at  $FUV_{AB} \sim 26$ .

3. We detect the optical counterparts (as identified by Barger et al. 2003) to six of 13 *Chandra* sources in the field. The FUV and X-ray properties of these sources are consistent with star formation rather than active galactic nuclei.

4. Eighteen FUV-detected galaxies are also detected in the GOODS MIPS  $24\ \mu\text{m}$  image of the field. The inferred ratio of infrared to ultraviolet luminosities,  $IRX$ , generally follows the relationship with UV-slope,  $\beta$ , measured for either starbursts Meurer et al. (1999) or normal galaxies Cortese et al. (2005). Using the  $IRX - \beta$  relation to correct for extinction, we infer star formation rates of a few tenths of a solar mass per year up to almost 10, for the entire sample of FUV detected sources. The median SFR is  $0.3\ M_{\odot}/\text{yr}$  and 75% of sources have  $\text{SFR} < 1\ M_{\odot}/\text{yr}$ .

5. Rest-frame  $B$ -band morphologies are available in the literature for most of the FUV-detected sources. Half of the FUV-detected sources have spiral morphologies. We detect only  $\sim 40\%$  of galaxies with irregular morphologies, which we attribute to their intrinsic faintness rather than unusually red color. We find evidence for star formation in  $\sim 50\%$  of the morphologically identified, moderate-mass spheroids at  $z < 0.85$ . These sources include the “blue-core” ellipticals with the strongest color gradients. As noted by Stanford et al. (2004), the morphologically-identified spheroids include sources with the SED of local ellipticals and other, bluer galaxies. The former group are generally not detected by our survey. Thus the SED of the spheroids supports our identification of the FUV flux as arising from ongoing star formation. The large fraction of FUV-detected spheroids suggests they continue to build stellar mass after  $z \sim 1$ , which is supported by their morphological asymmetries.

The small area of the HDF limits the results that can be drawn from the present survey. We have undertaken a complementary survey to obtain FUV imaging of the Hubble Ultra Deep Field (Beckwith et al. 2003), and results will be presented in a future paper. The combination of ultra-deep HST and GALEX imaging of the same fields will augment the interpretation of both.

The research described in this paper was carried out, in part, by the Jet Propulsion Laboratory, California Institute of Technology, and was sponsored by the National Aeronautics and Space Administration. Support for proposal 9478 was provided by NASA through a grant from STScI, which is operated by AURA, Inc., under NASA contract NAS 5-26555.

## REFERENCES

- Adelberger, K. L., & Steidel, C. C. 2000, *ApJ*, 544, 218
- Abraham, R. G., Ellis, R. S., Fabian, A. C., Tanvir, N. R., & Glazebrook, K. 1999, *MNRAS*, 303, 641
- Alexander, D. M., et al. 2003, *AJ*, 126, 539
- Appleton, P. N., et al. 2004, *ApJS*, 154, 147
- Barger, A. J., et al. 2003, *AJ*, 126, 632
- Beckwith, S. V. W., et al. 2003, American Astronomical Society Meeting Abstracts, 202,
- Bell, E. F., et al. 2004, *ApJ*, 608, 752
- Bertin, E., & Arnouts, S. 1996, *A&AS*, 117, 393
- Brown, T. M., Ferguson, H. C., Davidsen, A. F., & Dorman, B. 1997, *ApJ*, 482, 685
- Brown, T. M., Kimble, R. A., Ferguson, H. C., Gardner, J. P., Collins, N. R., & Hill, R. S. 2000a, *AJ*, 120, 1153
- Brown, T. M., Bowers, C. W., Kimble, R. A., & Ferguson, H. C. 2000b, *ApJ*, 529, L89
- Brown, T. M., Ferguson, H. C., Smith, E., Bowers, C. W., Kimble, R. A., Renzini, A., & Rich, R. M. 2003, *ApJ*, 584, L69
- Buat, V., Burgarella, D., Deharveng, J. M., & Kunth, D. 2002, *A&A*, 393, 33
- Buat, V., et al. 2005, *ApJ*, 619, L51
- Budavári, T., Szalay, A. S., Connolly, A. J., Csabai, I., & Dickinson, M. 2000, *AJ*, 120, 1588
- Burgarella, D., Buat, V., & Iglesias-Páramo, J. 2005, *MNRAS*, 360, 1413
- Calzetti, D., Kinney, A. L., & Storchi-Bergmann, T. 1994, *ApJ*, 429, 582
- Chary, R. & Elbaz, D. 2001, *ApJ*, 556, 562
- Cohen, J. G., Hogg, D. W., Blandford, R., Cowie, L. L., Hu, E., Songaila, A., Shopbell, P., & Richberg, K. 2000, *ApJ*, 538, 29
- Cohen, J. G. 2001, *AJ*, 121, 2895



- Conselice, C. J. 2003, *ApJS*, 147, 1
- Conselice, C. J., Bershad, M. A., Dickinson, M., & Papovich, C. 2003, *AJ*, 126, 1183
- Conselice, C. J., Blackburne, J. A., & Papovich, C. 2005, *ApJ*, 620, 564
- Cortese, L., et al. 2005, in press; astro-ph/0510165
- Cowie, L. L., Songaila, A., Hu, E. M., & Cohen, J. G. 1996, *AJ*, 112, 839
- Dale, D. A., & Helou, G. 2002, *ApJ*, 576, 159
- Dawson, S., Stern, D., Bunker, A. J., Spinrad, H., & Dey, A. 2001, *AJ*, 122, 598
- de Mello, D. F., Gardner, J. P., Dahlen, T., Conselice, C. J., Grogin, N. A., & Koekemoer, A. M. 2004, *ApJ*, 600, L151
- Dickinson, M., Papovich, C., Ferguson, H. C., & Budavári, T. 2003, *ApJ*, 587, 25
- Fazio, G. G., et al. 2004, *ApJS*, 154, 10
- Fernández-Soto, A., Lanzetta, K. M., & Yahil, A. 1999, *ApJ*, 513, 34
- Ferguson, H. C. 1998, in “The Hubble Deep Field”, ed. M. Livio, S. M. Fall, & P. Madau (Cambridge: Cambridge Univ. Press), 181
- Fitzpatrick, E. L. 1986, *AJ*, 92, 1068
- Flores, H., et al. 1999, *ApJ*, 517, 148
- Ford, H. C., et al. 1998, *Proc. SPIE*, 3356, 234
- Fruchter, A. S., & Hook, R. N. 2002, *PASP*, 114, 144
- Gardner, J. P., Brown, T. M., & Ferguson, H. C. 2000, *ApJ*, 542, L79; GBF
- Gardner, J. P., et al. 2000, *AJ*, 119, 486
- Goldader, J. D., Meurer, G., Heckman, T. M., Seibert, M., Sanders, D. B., Calzetti, D., & Steidel, C. C. 2002, *ApJ*, 568, 651
- Granato, G. L., Lacey, C. G., Silva, L., Bressan, A., Baugh, C. M., Cole, S., & Frenk, C. S. 2000, *ApJ*, 542, 710
- Hogg, D. W., Cohen, J. G., Blandford, R., & Pahre, M. A. 1998, *ApJ*, 504, 622

- Kennicutt, R. C. 1998, *ARA&A*, 36, 189
- Kimble, R. A., et al. 1998, *ApJ*, 492, L83
- Kinney, A. L., Bohlin, R. C., Calzetti, D., Panagia, N., & Wyse, R. F. G. 1993, *ApJS*, 86, 5
- Lilly, S. J., Le Fevre, O., Hammer, F., & Crampton, D. 1996, *ApJ*, 460, L1
- Madau, P., Ferguson, H. C., Dickinson, M. E., Giavalisco, M., Steidel, C. C., & Fruchter, A. 1996, *MNRAS*, 283, 1388
- Madau, P., Pozzetti, L., & Dickinson, M. 1998, *ApJ*, 498, 106
- Marcillac, D., et al. 2005, *A&A*, submitted
- Martin, D. C., et al. 2005, *ApJ*, 619, L1
- Menanteau, F., Abraham, R. G., & Ellis, R. S. 2001, *MNRAS*, 322, 1
- Menanteau, F., et al. 2005, *ApJ*, 620, 697
- Meurer, G. R., Heckman, T. M., & Calzetti, D. 1999, *ApJ*, 521, 64
- Milliard, B., Donas, J., Laget, M., Armand, C., & Vuillemin, A. 1992, *A&A*, 257, 24
- Oke, J. B. 1971, *ApJ*, 170, 193
- Papovich, C., Giavalisco, M., Dickinson, M., Conselice, C. J., & Ferguson, H. C. 2003, *ApJ*, 598, 827
- Ranalli, P., Comastri, A., & Setti, G. 2003, *A&A*, 399, 39
- Rieke, G. H., et al. 2004, *ApJS*, 154, 25
- Salpeter, E. E. 1955, *ApJ*, 121, 161
- Sasseen, T. P., Eisenman, I., Mason, K., & the XMM Optical Monitor Team 2002; *astro-ph/0204322*
- Schiminovich, D., et al. 2005, *ApJ*, 619, L47
- Seibert, M., et al. 2005, *ApJ*, 619, L55
- Somerville, R. S., Lee, K., Ferguson, H. C., Gardner, J. P., Moustakas, L. A., & Giavalisco, M. 2004, *ApJ*, 600, L171

- Soifer, B. T., Sanders, D. B., Madore, B. F., Neugebauer, G., Danielson, G. E., Elias, J. H., Lonsdale, C. J., & Rice, W. L. 1987, *ApJ*, 320, 238
- Stanford, S. A., Dickinson, M., Postman, M., Ferguson, H. C., Lucas, R. A., Conselice, C. J., Budavári, T., & Somerville, R. 2004, *AJ*, 127, 131
- Trager, S. C., Faber, S. M., Worthey, G., & González, J. J. 2000, *AJ*, 120, 165
- Treyer, M., et al. 2005, *ApJ*, 619, L19
- Williams, R. E., et al. 1996, *AJ*, 112, 1335
- Wilson, G., Cowie, L. L., Barger, A. J., & Burke, D. J. 2002, *AJ*, 124, 1258
- Windhorst, R. A., et al. 2002, *ApJS*, 143, 113
- Wolf, C., et al. 2005, *ApJ*, 630, 771
- Woodgate, B. E., et al. 1998, *PASP*, 110, 1183
- Xu, C. K., et al. 2005, *ApJ*, 619, L11
- Yi, S. K., et al. 2005, *ApJ*, 619, L111

Table 1. Photometry

Object	R.A. <sup>a</sup> (J2000)	Dec <sup>a</sup> (J2000)	Inst <sup>b</sup>	FUV <sub>AB</sub> (mag.)	$\sigma_{FUV}$ (mag.)	HDF ID <sup>c</sup>
1	12:36:39.77	62:12:28.75	S	25.98	0.16	4-852.0
2	12:36:39.87	62:12:31.61	S	27.93	0.36	4-823.0
3	12:36:40.05	62:12:21.43	S	27.00	0.22	4-860.1
4	12:36:40.09	62:12:22.24	S	26.57	0.14	4-860.0
5	12:36:41.15	62:12:10.59	S	27.97	0.34	4-822.0
6	12:36:41.95	62:12: 5.40	S	24.62	0.09	4-795.0
7	12:36:42.92	62:12:16.37	S	24.19	0.04	4-656.0
8	12:36:43.40	62:13: 4.76	A	27.66	0.24	1-43.0
9	12:36:43.41	62:11:49.27	S	28.26	0.53	4-728.0
10	12:36:43.63	62:12:18.24	S	27.70	0.45	4-565.0
11	12:36:43.82	62:12:22.41	S	28.26	0.31	4-525.0
12	12:36:43.98	62:12:49.92	A	26.45	0.26	4-402.31
13	12:36:44.18	62:12:47.78	A	24.15	0.03	4-402.0
14	12:36:44.47	62:13: 7.63	A	27.98	0.16	1-41.0
15	12:36:44.48	62:11:53.26	S	27.86	0.30	4-627.0
16	12:36:44.62	62:13:18.94	A	27.66	0.16	1-76.0
17	12:36:44.70	62:13: 6.74	A	27.52	0.16	1-37.2
18	12:36:44.73	62:11:43.81	S	26.81	0.16	4-658.0
19	12:36:44.74	62:11:57.06	S	26.65	0.12	4-579.0
20	12:36:44.82	62:13:17.57	A	27.80	0.16	1-68.0
21	12:36:44.83	62:12: 0.25	S	25.32	0.08	4-558.0
22	12:36:45.31	62:11:42.91	S	26.17	0.10	4-618.0
23 <sup>h</sup>	12:36:45.42	62:12:13.55	S	23.60	0.03	4-454.0
24	12:36:45.43	62:13:26.01	A	24.76	0.04	1-86.0
25 <sup>d</sup>	12:36:45.47	62:13:56.99	A	27.54	0.15	2-126.0
26	12:36:45.51	62:13:44.14	A	26.41	0.10	2-62.0
27	12:36:45.54	62:13:29.95	A	27.06	0.12	1-100.0
28	12:36:45.63	62:13: 8.89	A	26.26	0.08	1-35.0
29	12:36:45.86	62:13:25.82	A	23.80	0.03	1-87.0
30	12:36:45.91	62:13:44.82	A	26.69	0.10	2-100.0
31	12:36:45.96	62:12: 1.41	S	27.42	0.23	4-460.0
32	12:36:46.12	62:13:34.71	A	27.43	0.17	2-61.0
33	12:36:46.16	62:13:13.93	A	26.69	0.09	1-47.0
34	12:36:46.36	62:14: 4.99	A	28.25	1.19	2-251.0
35	12:36:46.55	62:14: 7.60	A	25.40	0.05	2-270.0
36	12:36:46.55	62:12: 3.10	S	26.02	0.09	4-416.0
37	12:36:46.58	62:11:57.16	S	26.87	0.15	4-434.0
38	12:36:46.75	62:13:12.31	A	26.08	0.09	2-7.0
39	12:36:46.95	62:12: 5.37	S	27.46	0.24	4-382.0
40	12:36:46.96	62:13:27.84	A	26.31	0.15	2-108.0
41	12:36:47.02	62:13:52.99	A	26.55	0.09	2-231.0
42	12:36:47.05	62:12:36.87	A	23.07	0.02	4-241.1
43	12:36:47.08	62:12:12.54	S	27.17	0.18	4-332.0
44	12:36:47.15	62:14:15.96	A	27.28	0.12	2-354.0
45	12:36:47.23	62:11:58.96	S	27.55	0.21	4-385.0

Table 1—Continued

Object	R.A. <sup>a</sup> (J2000)	Dec <sup>a</sup> (J2000)	Inst <sup>b</sup>	FUV <sub>AB</sub> (mag.)	$\sigma_{FUV}$ (mag.)	HDF ID <sup>c</sup>
46	12:36:47.25	62:12:12.66	A	27.34	0.11	4-332.2
47	12:36:47.28	62:12:30.81	A	24.69	0.04	4-232.0
48	12:36:47.41	62:14: 3.05	A	25.69	0.06	2-321.1
49	12:36:47.54	62:12:52.68	A	27.13	0.13	4-89.0
50	12:36:47.73	62:13:14.39	A	28.77	0.22	2-88.0
51	12:36:47.84	62:13: 6.48	A	28.25	0.23	2-121.2
52	12:36:47.89	62:12:29.49	A	28.23	0.27	4-174.0
53	12:36:47.94	62:13:11.08	A	27.89	0.16	2-121.12
54	12:36:47.98	62:13:31.93	A	28.18	0.18	2-197.0
55	12:36:48.13	62:12:14.88	A	26.07	0.06	4-260.0
56 <sup>e</sup>	12:36:48.31	62:14:26.45	A	20.95	0.01	2-537.0
57	12:36:48.63	62:12:14.13	A	26.91	0.13	4-260.2
58	12:36:48.73	62:13: 2.48	A	28.73	0.34	3-51.0
59	12:36:48.78	62:13:18.60	A	26.44	0.13	2-210.0
60	12:36:48.92	62:12: 8.02	A	27.80	0.21	4-203.0
61	12:36:49.00	62:12:45.84	A	25.86	0.13	3-258.0
62	12:36:49.35	62:11:54.97	A	28.26	0.22	4-235.0
63	12:36:49.39	62:13:11.27	A	25.22	0.05	2-264.0
64 <sup>i</sup>	12:36:49.45	62:13:46.85	A	25.82	0.23	2-456.0
65	12:36:49.50	62:14: 6.69	A	27.12	0.17	2-514.0
66	12:36:49.59	62:14:14.99	A	27.99	0.27	2-585.2
67	12:36:49.63	62:12:57.79	A	25.66	0.06	3-143.0
68	12:36:49.77	62:13:13.03	A	26.39	0.12	2-264.1
69	12:36:49.89	62:12:42.17	A	27.41	0.24	3-331.0
70	12:36:50.11	62:14:28.68	A	28.74	0.19	2-681.0
71	12:36:50.17	62:14:22.16	A	26.81	0.09	2-645.0
72	12:36:50.23	62:14: 7.62	A	26.81	0.10	2-575.0
73	12:36:50.24	62:12:39.55	A	23.41	0.02	3-386.0
74	12:36:50.29	62:12:53.45	A	28.98	0.22	3-201.0
75	12:36:50.80	62:12:21.36	A	26.46	0.08	3-599.0
76	12:36:50.82	62:12: 0.81	A	27.19	0.12	4-71.0
77	12:36:50.83	62:12:55.88	A	24.09	0.03	3-203.0
78	12:36:50.84	62:12:51.54	A	25.20	0.05	3-259.0
79	12:36:50.84	62:12:27.24	A	27.44	0.18	3-528.0
80	12:36:51.03	62:12:54.75	A	27.56	0.15	3-208.0
81	12:36:51.06	62:13:20.60	A	21.71	0.02	2-404.0
82	12:36:51.44	62:13: 0.26	A	24.16	0.04	3-174.0
83	12:36:51.71	62:12:20.25	A	25.92	0.09	3-659.0
84	12:36:51.76	62:13:53.81	A	26.13	0.14	2-652.0
85 <sup>d</sup>	12:36:51.95	62:11:55.53	A	25.47	0.08	3-956.0
86	12:36:51.96	62:12:30.52	A	28.75	0.20	3-523.0
87	12:36:52.02	62:12: 9.72	A	24.78	0.04	3-777.0
88	12:36:52.03	62:14: 0.96	A	26.58	0.10	2-702.0
89	12:36:52.21	62:13:23.34	A	27.74	0.24	2-486.0
90	12:36:52.23	62:13:48.06	A	27.03	0.12	2-646.0

Table 1—Continued

Object	R.A. <sup>a</sup> (J2000)	Dec <sup>a</sup> (J2000)	Inst <sup>b</sup>	FUV <sub>AB</sub> (mag.)	$\sigma_{FUV}$ (mag.)	HDF ID <sup>c</sup>
91	12:36:52.36	62:13:46.68	A	28.71	0.25	2-640.0
92	12:36:52.69	62:12:19.69	A	25.33	0.05	3-696.0
93 <sup>f</sup>	12:36:52.78	62:13:56.07	A	27.67	0.14	2-736.2
94	12:36:52.91	62:14: 8.51	A	26.96	0.10	2-834.0
95	12:36:52.98	62:12:56.76	A	26.70	0.09	3-271.0
96	12:36:53.11	62:12:56.95	A	26.36	0.13	3-271.1
97	12:36:53.23	62:13:43.60	A	27.89	0.21	2-712.0
98	12:36:53.33	62:13: 0.59	A	27.54	0.15	3-227.0
99 <sup>d</sup>	12:36:53.39	62:13:25.05	A	27.99	0.20	2-619.0
100	12:36:53.46	62:12:34.23	A	26.38	0.09	3-551.0
101	12:36:53.48	62:12:20.61	A	26.48	0.12	3-708.0
102	12:36:53.49	62:12:10.93	A	27.81	0.27	3-801.0
103 <sup>g</sup>	12:36:54.03	62:12:45.70	A	27.07	0.12	3-419.0
104	12:36:54.71	62:13: 9.35	A	28.57	0.21	3-170.0
105	12:36:54.73	62:13:30.33	A	27.14	0.20	2-802.112
106	12:36:54.79	62:12:58.19	A	27.71	0.21	3-318.0
107	12:36:55.01	62:13:14.75	A	25.92	0.07	3-132.0
108	12:36:55.07	62:13:29.13	A	27.92	0.07	2-802.1112
109	12:36:55.14	62:13:11.36	A	24.81	0.03	3-180.2
110	12:36:55.25	62:12:52.43	A	26.07	0.10	3-398.0
111	12:36:55.27	62:13: 9.50	A	28.18	0.19	3-187.0
112	12:36:55.42	62:12:27.95	A	28.36	0.25	3-695.0
113	12:36:55.59	62:13:59.89	A	26.34	0.11	2-1018.0
114	12:36:55.78	62:13:48.78	A	28.11	0.26	2-966.0
115	12:36:56.11	62:12:41.25	A	28.04	0.18	3-610.111112
116	12:36:56.41	62:12: 9.22	A	25.24	0.05	3-943.0
117	12:36:56.63	62:12:44.71	A	25.32	0.19	3-610.1111111
118	12:36:56.95	62:12:58.24	A	26.90	0.18	3-404.0
119	12:36:57.23	62:12:25.87	A	24.42	0.04	3-773.0
120	12:36:57.32	62:12:59.71	A	23.20	0.02	3-400.0
121	12:36:57.36	62:12:56.24	A	27.16	0.17	3-412.0
122 <sup>f</sup>	12:36:57.46	62:12:12.00	A	25.11	0.04	3-965.111112
123	12:36:57.53	62:13:16.82	A	26.91	0.10	3-184.0
124	12:36:58.00	62:12:25.04	A	27.66	0.17	3-793.0
125	12:36:58.01	62:12:35.54	A	27.32	0.22	3-698.0
126	12:36:58.07	62:13: 0.34	A	23.73	0.02	3-405.0
127	12:36:58.17	62:13: 6.49	A	26.01	0.07	3-342.0
128	12:36:58.31	62:12:51.09	A	28.22	0.06	3-534.12
129	12:36:58.32	62:12:55.39	A	27.82	0.16	3-454.12
130	12:36:58.36	62:12:56.34	A	26.78	0.10	3-454.0
131	12:36:58.65	62:12:21.64	A	26.42	0.10	3-863.0
132	12:36:58.70	62:12:17.04	A	27.67	0.20	3-923.0
133 <sup>d</sup>	12:36:58.76	62:12:52.46	A	23.36	0.03	3-534.0
134	12:36:59.38	62:12:21.68	A	25.75	0.08	3-908.1
135	12:36:59.53	62:12:21.11	A	26.83	0.13	3-908.0

Table 1—Continued

Object	R.A. <sup>a</sup> (J2000)	Dec <sup>a</sup> (J2000)	Inst <sup>b</sup>	FUV <sub>AB</sub> (mag.)	$\sigma_{FUV}$ (mag.)	HDF ID <sup>c</sup>
--------	------------------------------	-----------------------------	-------------------	-----------------------------	--------------------------	---------------------

<sup>a</sup>Far-UV flux weighted position within HDF WFPC2 isophote

<sup>b</sup>A = ACS/SBC; S = STIS

<sup>c</sup>from catalog of (Williams et al. 1996)

<sup>d</sup>ies on the edge of the far-UV image.

<sup>e</sup>ies on the edge of the NICMOS images.

<sup>f</sup>NICMOS aperture includes multiple sources.

<sup>g</sup>WFPC2 aperture includes multiple sources.

<sup>h</sup>Star

<sup>i</sup><sub>z</sub>=0.089 elliptical. The FUV flux is limited to a much smaller aperture than the measured in the WFPC2 filters. The F300W flux likely to be dominated by older stars.

Table 2. SBC number counts

$FUV_{AB}$ (mag.)	n.c. $N(\text{deg}^{-2} \text{ mag}^{-1})$	low	high	Raw N
19.5000	...	...	...	0
20.5000	1077	186	3553	1
21.5000	1089	188	3594	1
22.5000	...	...	...	0
23.5000	6202	3915	9543	6
24.5000	7890	5160	11787	8
25.5000	17103	12870	22533	17
26.5000	31595	25954	38357	31
27.5000	39479	32745	47485	34
28.5000	32524	23929	43745	14



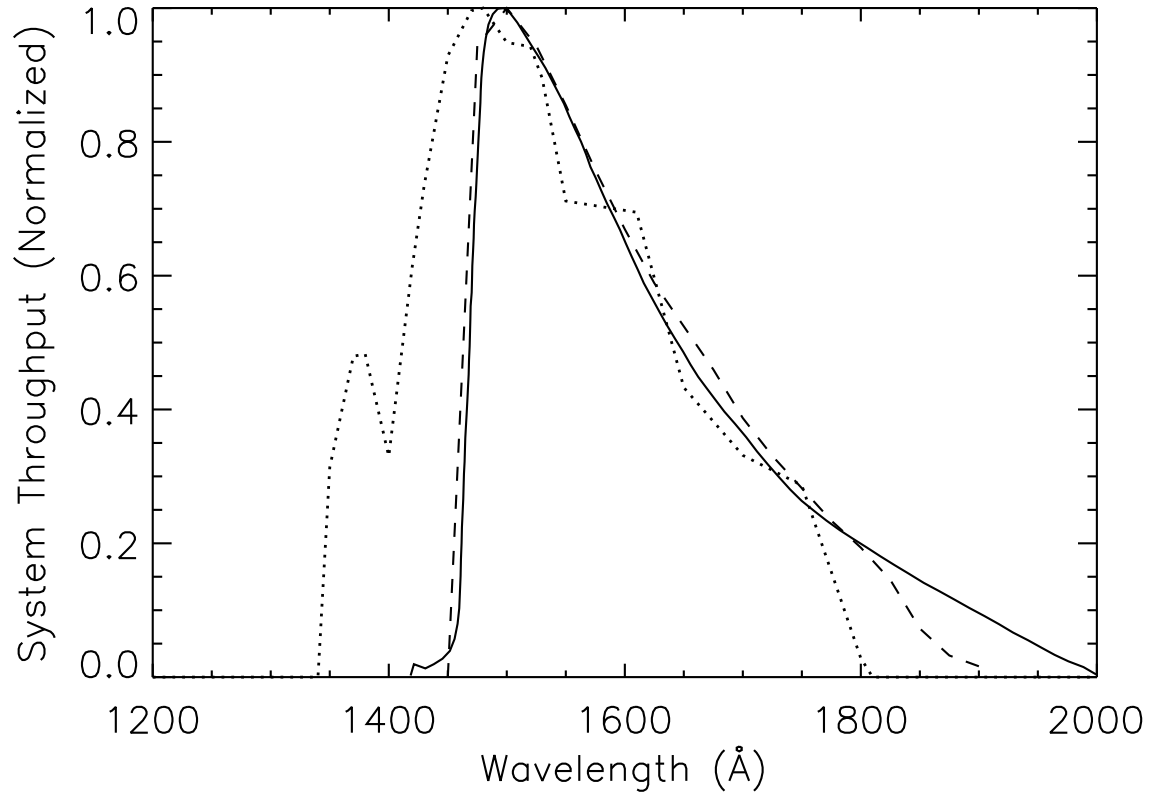


Fig. 1.— Total system throughput (filter+detector) for ACS/SBC F150LP (solid), STIS/FUVMAMA F25QTZ (dashed), and GALEX-FUV (dotted).

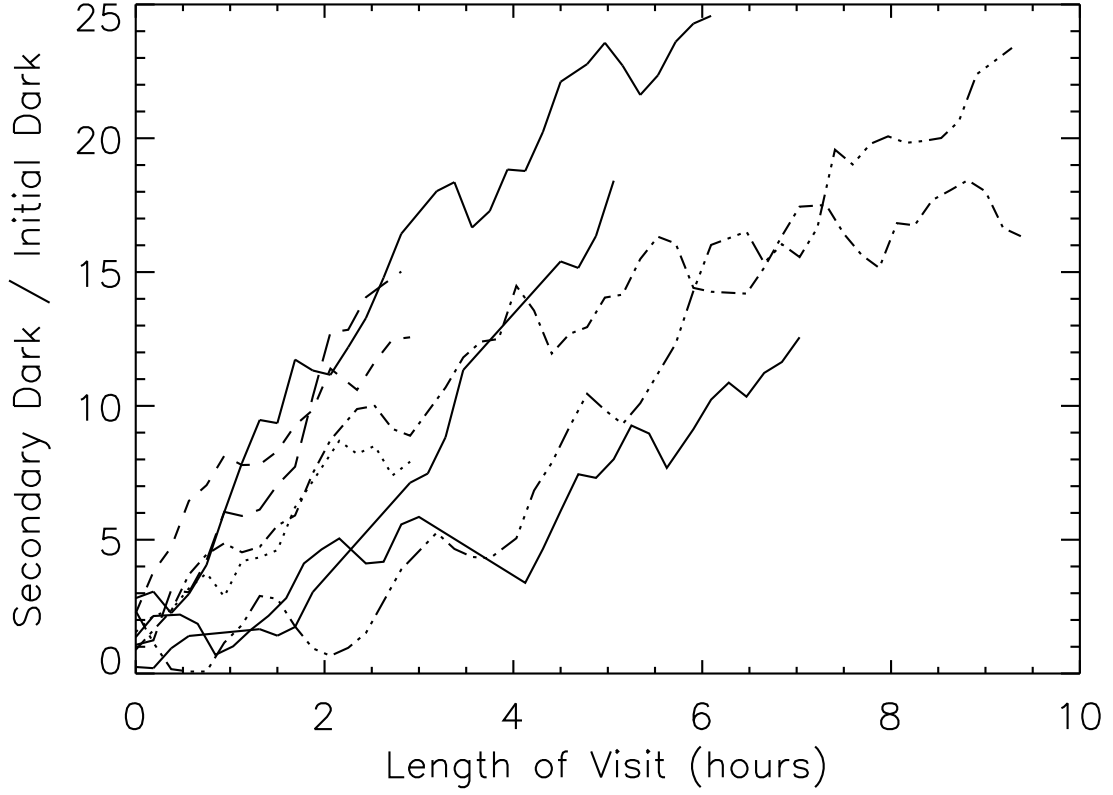


Fig. 2.— Count rate of the dark “glow” scaled to the dark rate at  $T < 20C$  ( $\sim 8 \times 10^{-6}$  counts  $s^{-1}$  pixel $^{-1}$ ) vs. time elapsed since the beginning of the visit. Each line denotes a different visit to the field. The count rate increases linearly with time at  $\sim 2.5 \times 10^{-5}$  counts $^{-1}$  s $^{-1}$  pixel $^{-1}$  hour $^{-1}$ .

Fig. 3.— A color composite of the FUV and F450W images of the HDF. The background image is the WFPC2 F450W image, over which the FUV data from STIS and ACS/SBC are shown in magenta.

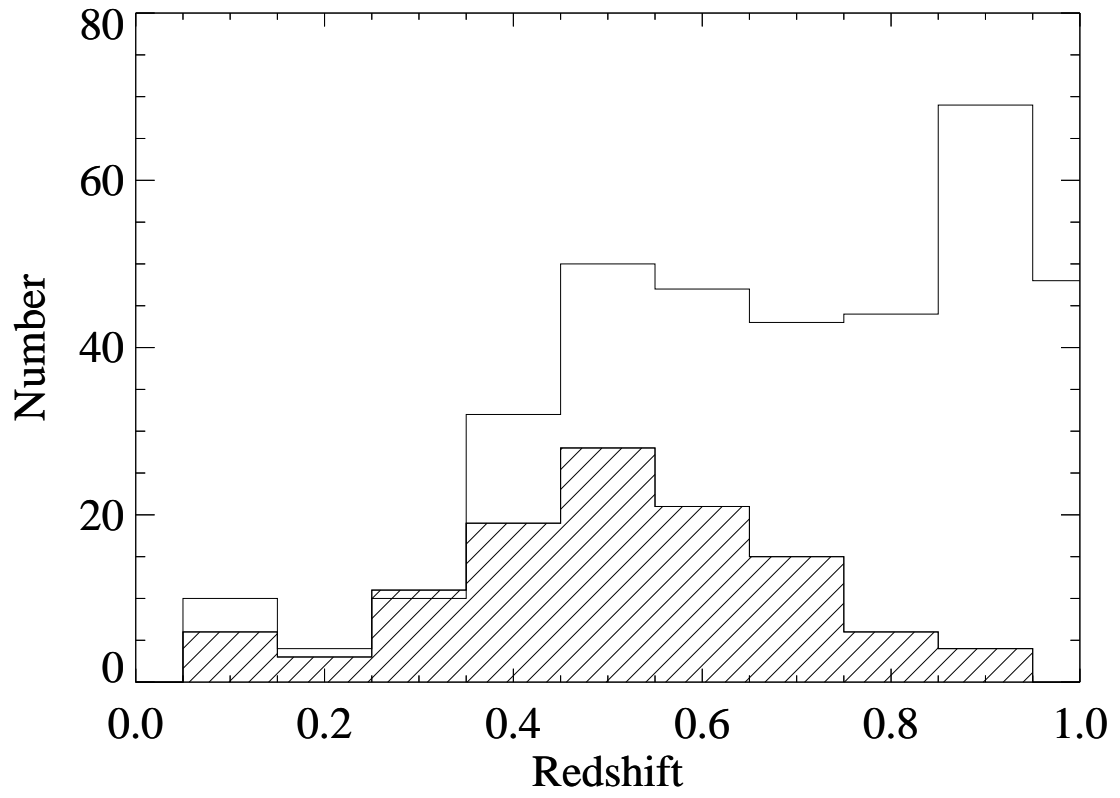


Fig. 4.— Distribution of redshifts. We plot the distribution of redshifts for NICMOS-selected sources in the HDF-N (solid line) and FUV-detections (filled histogram).

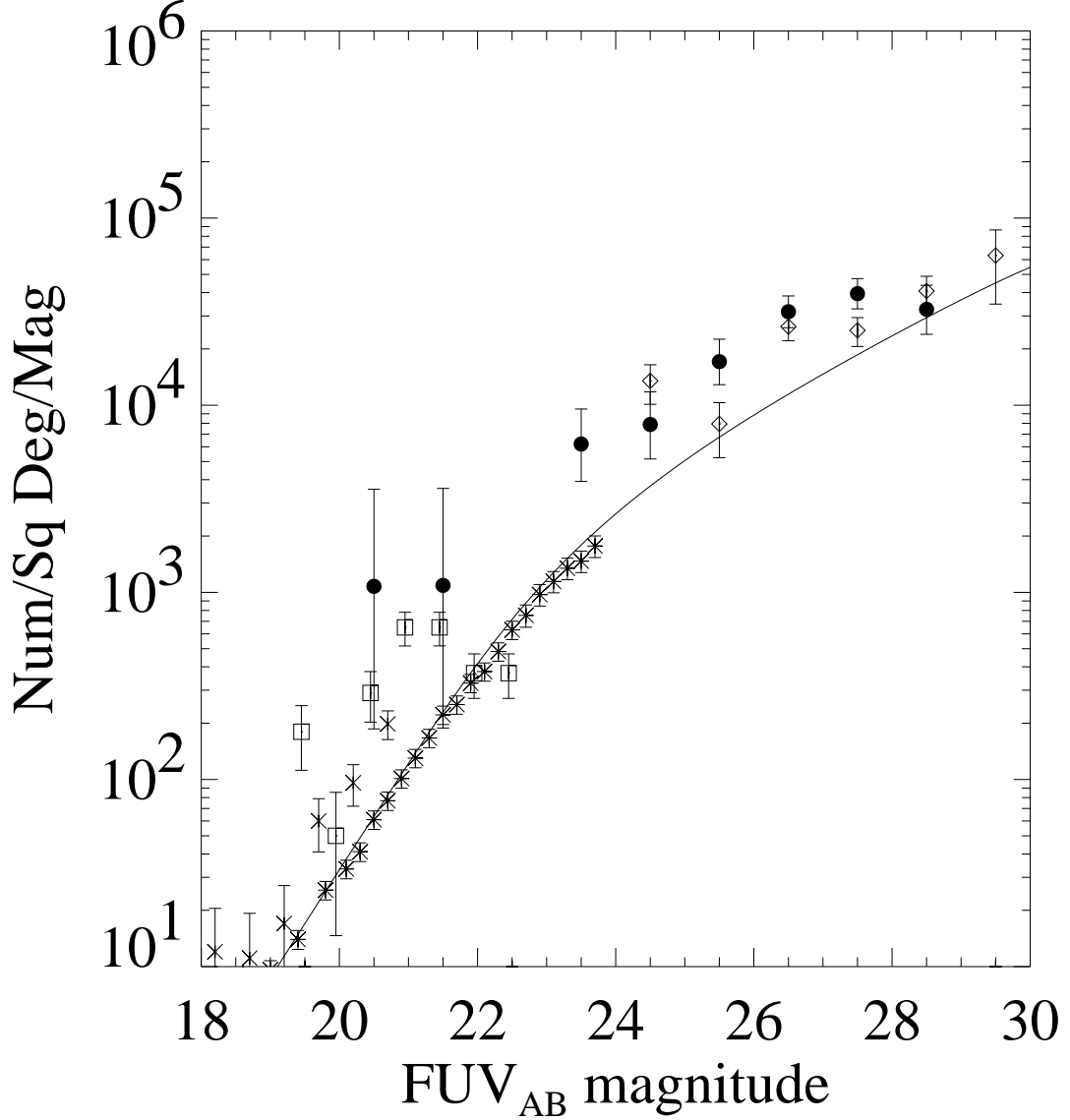


Fig. 5.— FUV number counts. We plot the galaxy number-magnitude counts for the ACS (solid symbols) and STIS (Gardner et al. 2000a, open symbols; ) sources. The STIS counts include seven fields of view near the HDF-North and a single pointing in the HDF-South data. We plot for comparison the XMM (squares; Sasseen et al. 2002) and FOCA (X's; Milliard et al. 1992) counts, corrected from 2000 Å to 1500 Å assuming a slope  $\beta = -0.8$ . We also plot the GALEX number counts (asterisks) without a color correction for filter differences, and their model fit which is closest to the HST counts (Xu et al. 2005).

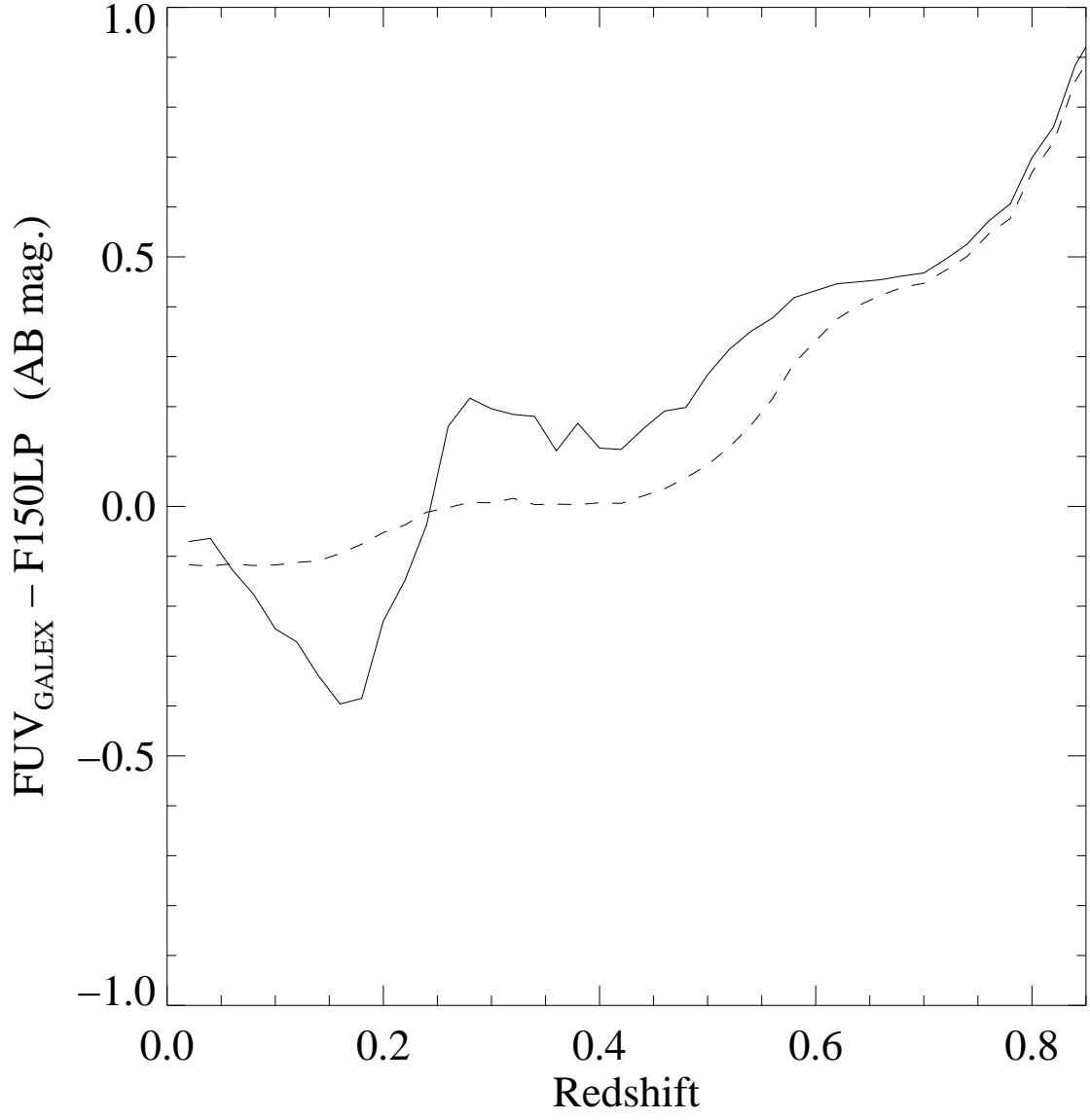


Fig. 6.— The color correction between the GALEX FUV filter and the ACS F150LP filter for sources with Ly $\alpha$  emission (solid line) and without it (dashed line). The color correction was calculated based on the template spectra of Kinney et al. (1993).

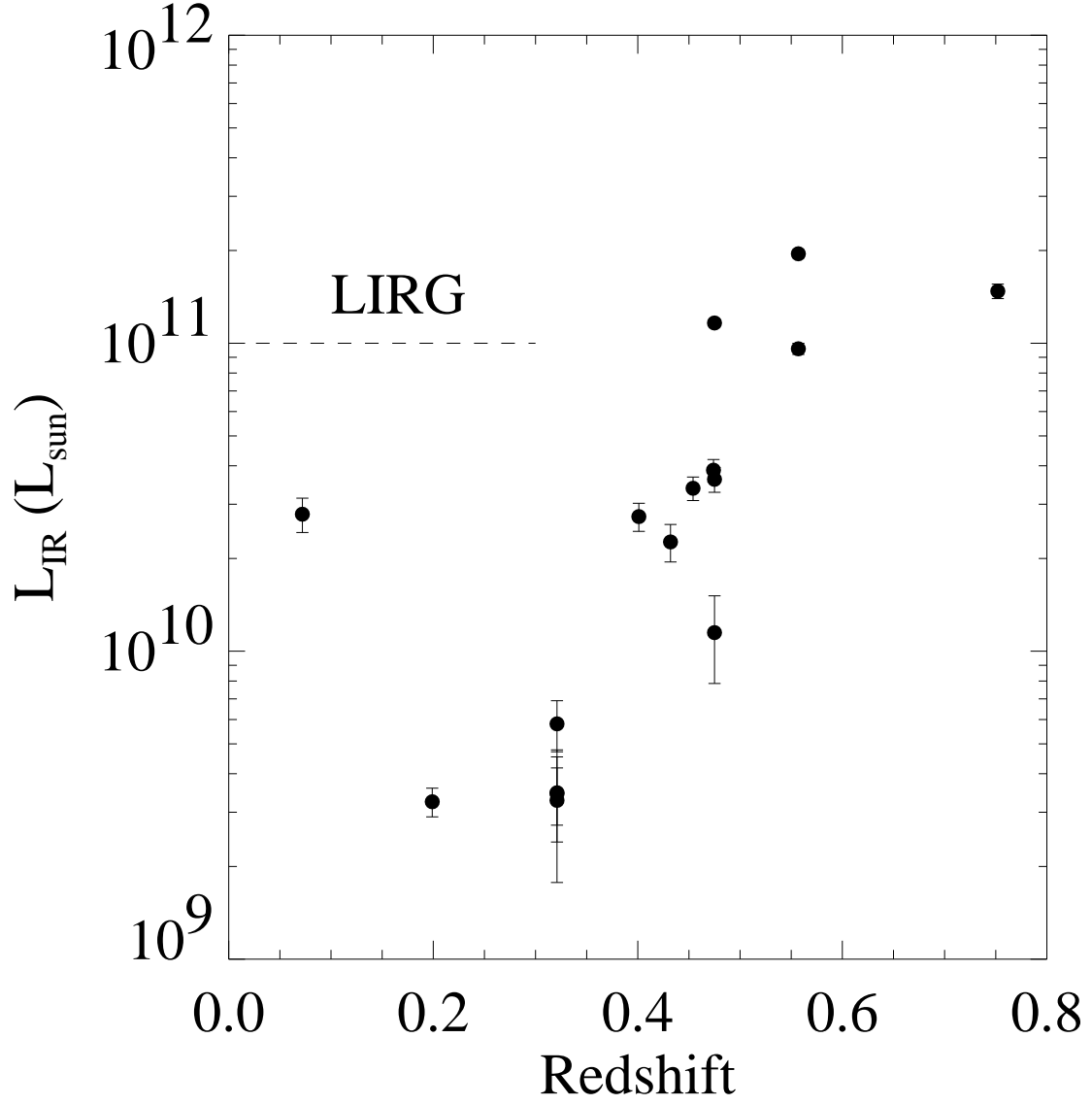


Fig. 7.— The inferred  $L_{IR}$  of MIPS counterparts to FUV sources. The errorbars include MIPS photometric uncertainty and a systematic term estimated from the difference between Chary & Elbaz (2001) and Dale & Helou (2002) templates.

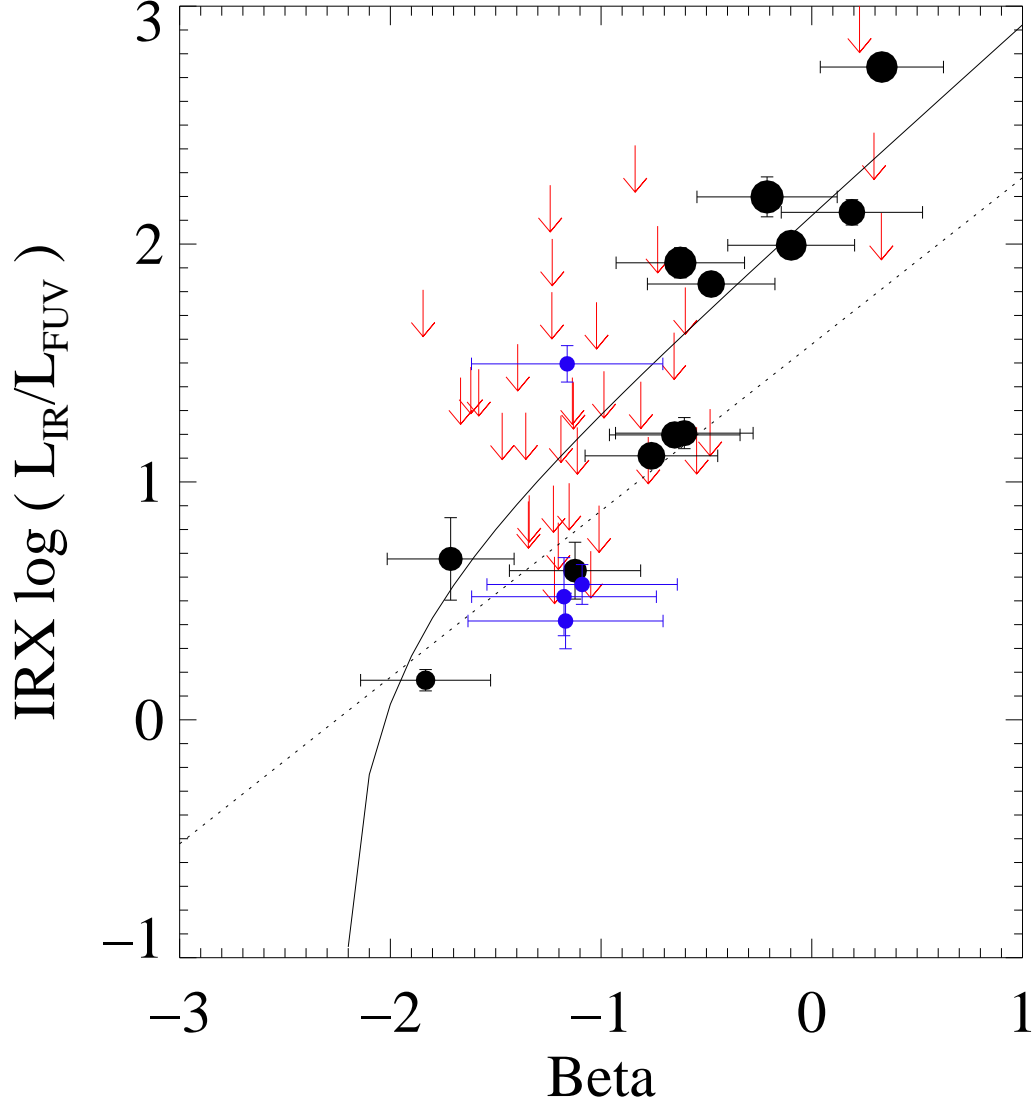


Fig. 8.— The ratio of inferred  $L_{\text{IR}}$  vs. UV luminosity ( $\nu f_\nu$ ), IRX, is plotted against the UV slope,  $\beta$ . The symbol size is proportional to the inferred  $L_{\text{IR}}$  (larger symbols for more luminous objects). Two  $\sigma$  upper limits are plotted for objects with IRAC counterparts but without 2 $\sigma$  MIPS detections. Error bars include statistical and systematic uncertainties as described in the text. Objects at  $0.2 < z < 0.4$  have higher uncertainty in the measurement of  $\beta$  and are plotted in blue. The solid line indicates the the relationship determined by Meurer et al. (1999) and the dotted line indicates the relationship measured by Cortese et al. (2005) for normal star-forming galaxies.



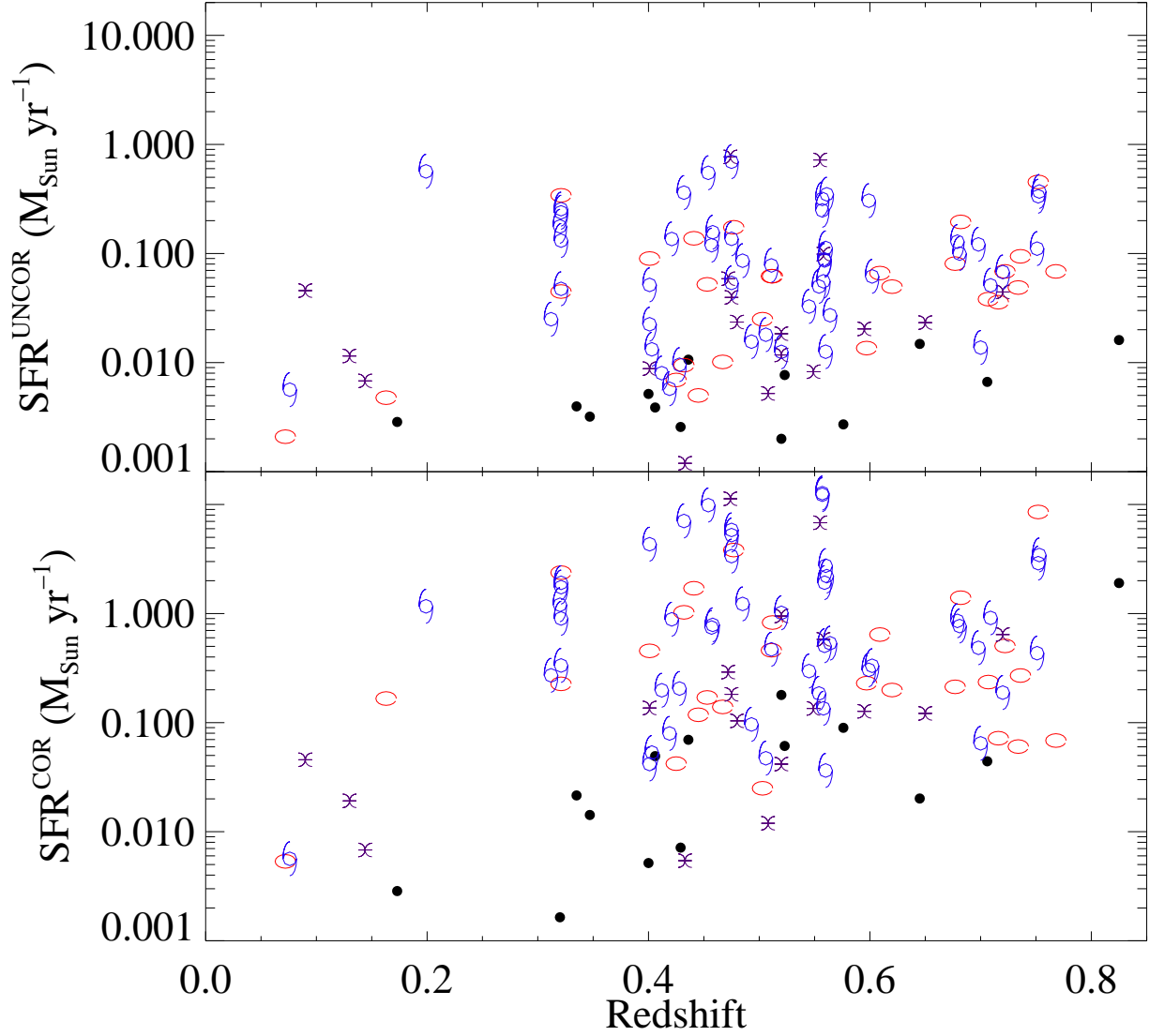


Fig. 9.— The inferred star formation rates for FUV detected sources, with (bottom) and without (top) extinction correction,  $A_{FUV}$ . Morphological type are indicated by symbols: red ellipses for E/0, purple stylized asterisk for peculiar/irregular, blue stylized spiral for later than S0, and solid circles for objects too faint to classify. Classifications were performed by eye in the rest frame B-band (Conselice et al. 2005) as described in Section 4.3.

Fig. 10.— The morphological K-correction. We compare the UV morphology of galaxies at different redshifts to their appearance in WFPC2 F300W and F814W bands, as well as the NICMOS F160W. The FUV and F300W data have been smoothed with a Gaussian kernel corresponding to the FWHM of a point source.

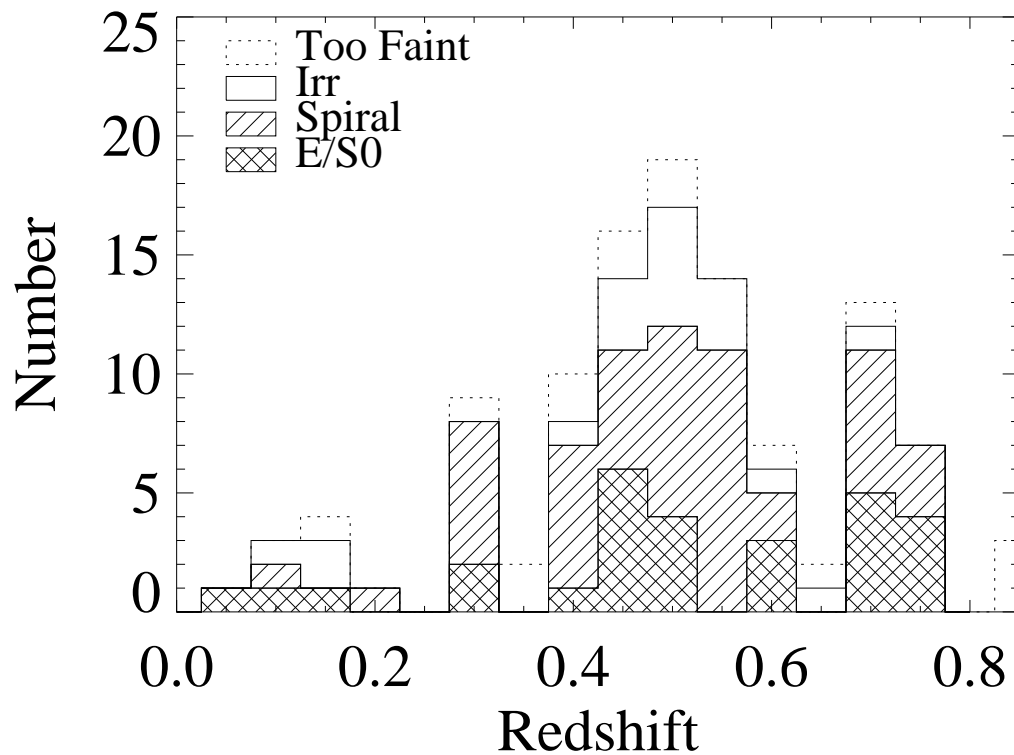


Fig. 11.— The distribution of redshifts for each morphological type. Classifications were performed by eye in the rest frame B-band (see text).

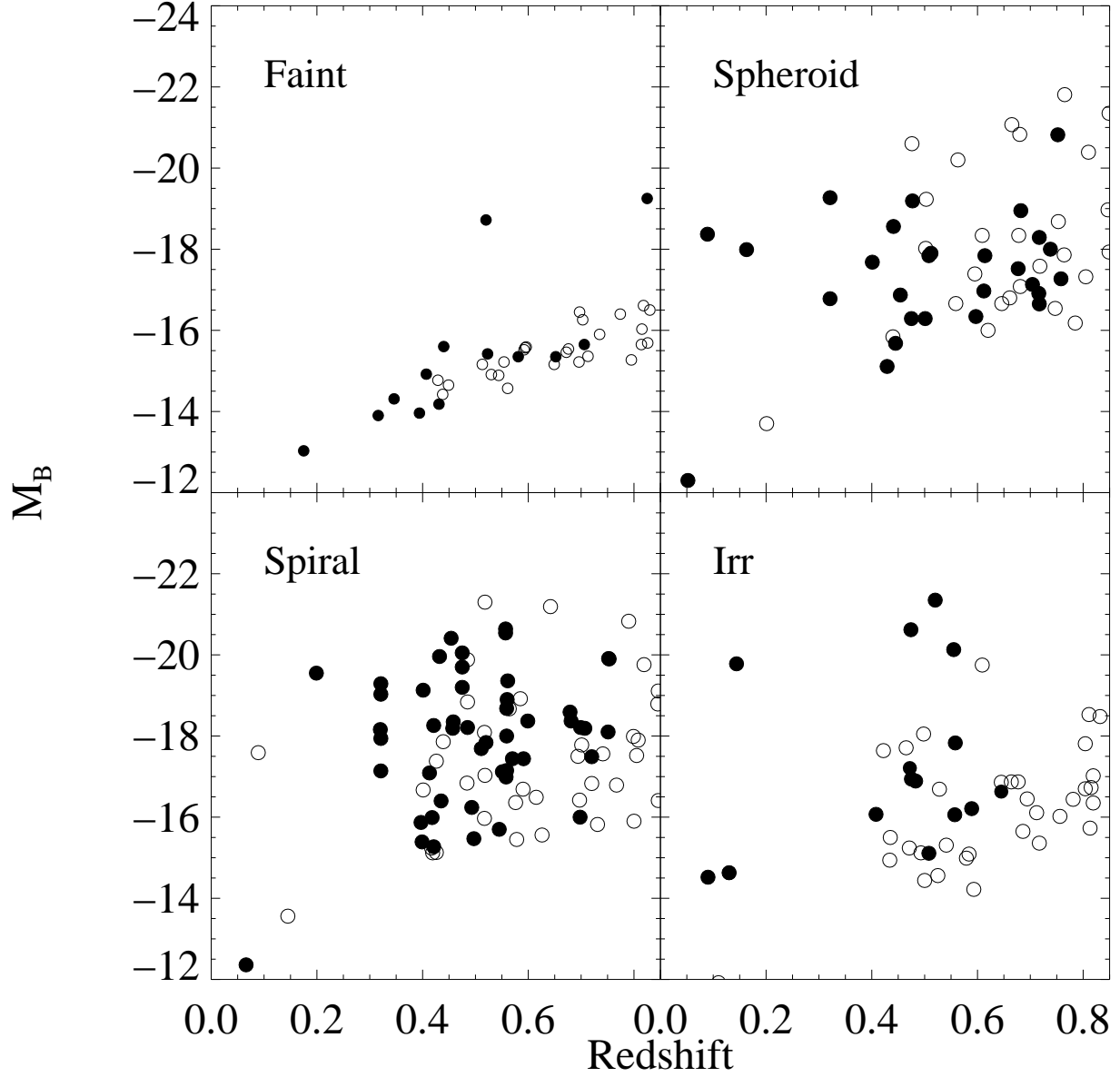


Fig. 12.— Absolute magnitude as a function of redshift. We plot  $z$  vs.  $M_B$  for each morphological type: spheroids (upper right), peculiar/irregular (lower right), later than S0 (lower left), and objects too faint to classify (upper left). Classifications were performed by eye in the rest frame B-band (Conselice et al. 2005, see text). Objects detected in the FUV are plotted with filled circles.

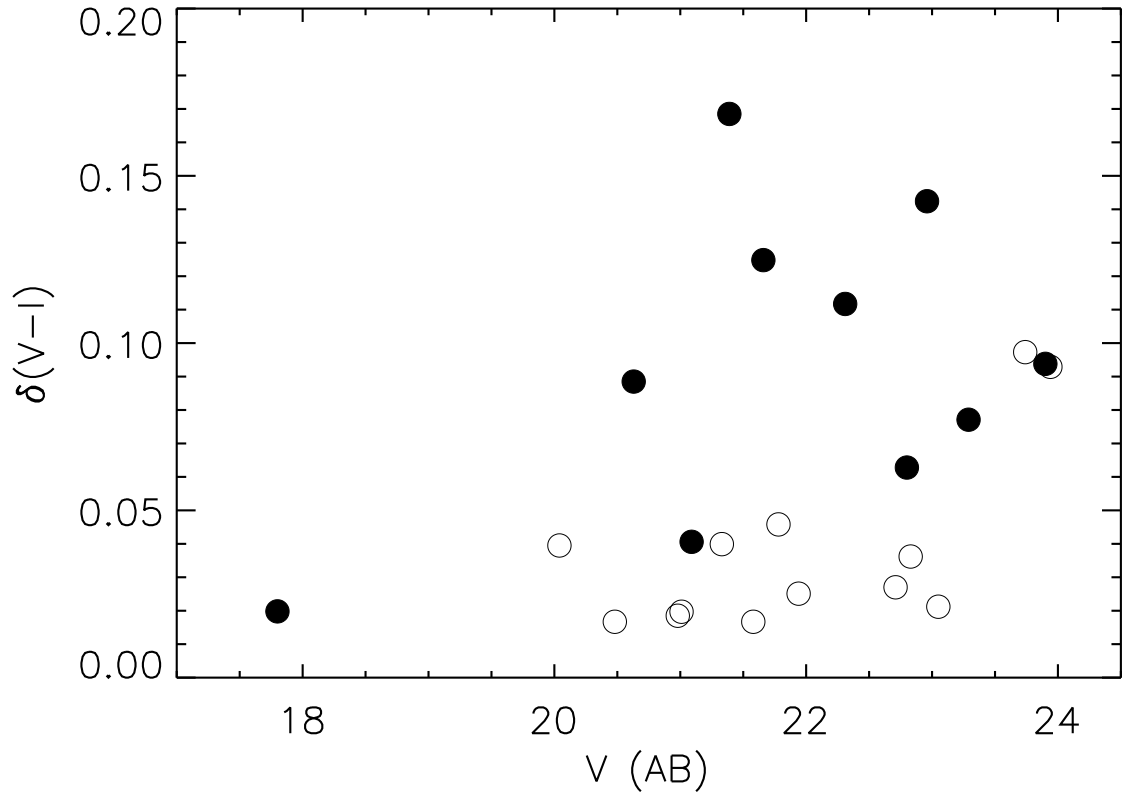


Fig. 13.— FUV detection of blue core ellipticals. We plot the color gradient for ellipticals identified in Menanteau et al. (2001) vs. their  $F450W$  magnitude. A larger color gradient indicates a bluer object. Filled symbols indicate FUV detection.

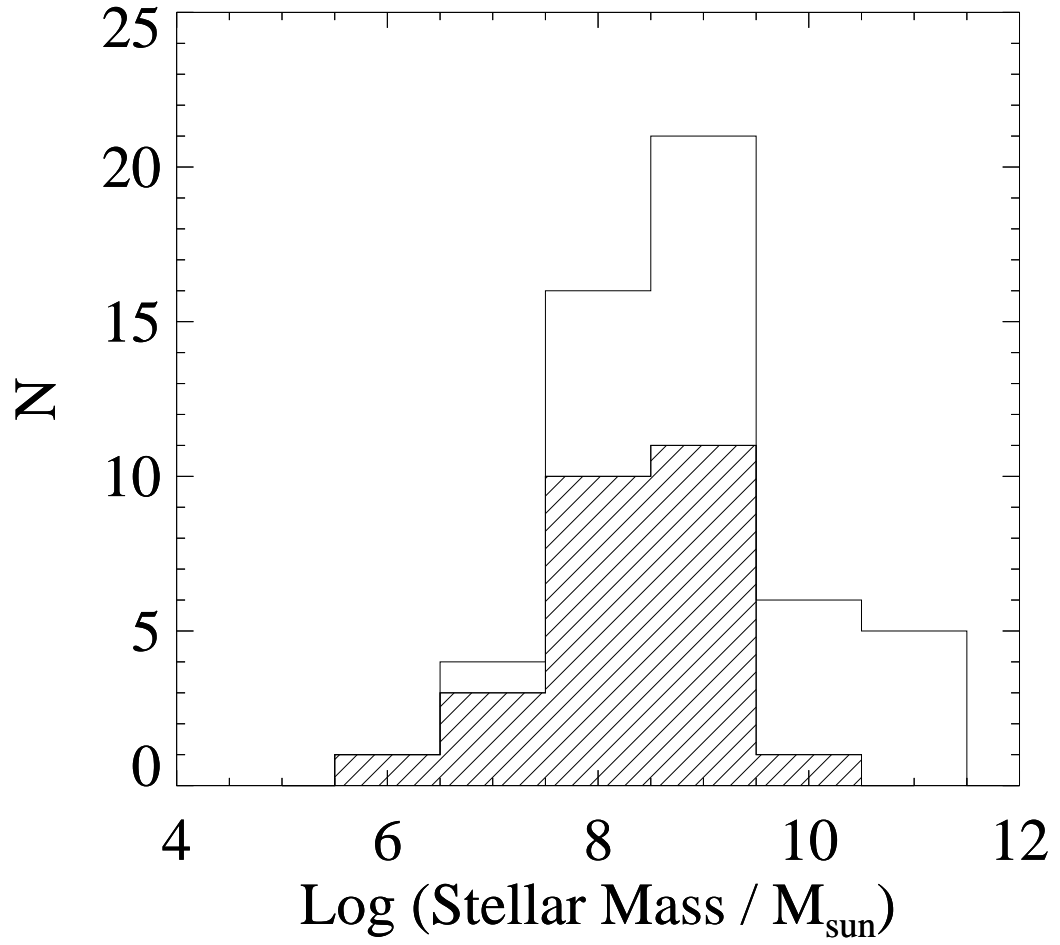


Fig. 14.— Histogram of distribution of inferred mass for spheroids in the HDF. Sources detected in the FUV are shown by the hatched histogram.

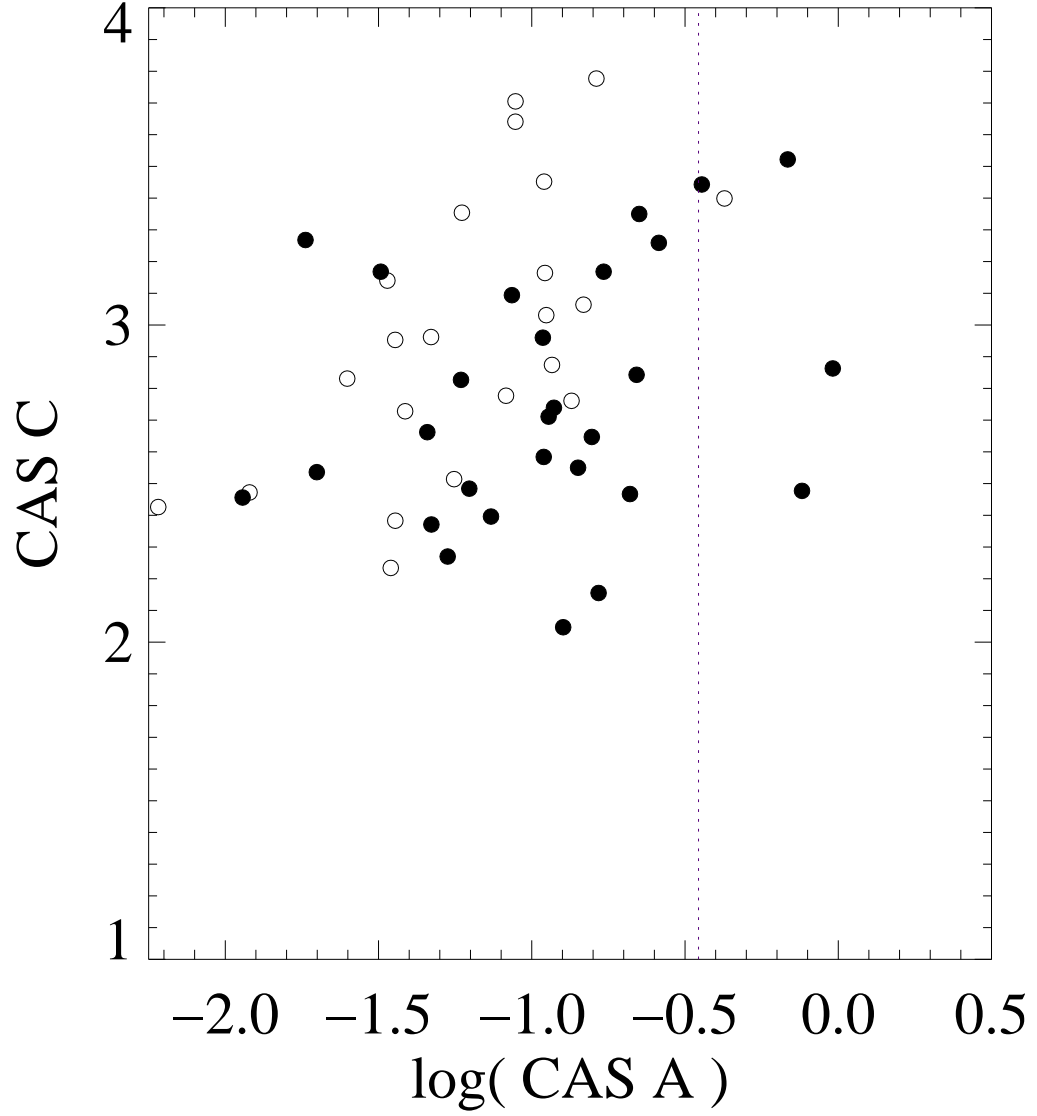


Fig. 15.— The concentration and asymmetry plane for spheroids at  $z < 0.85$  in the HDF (Conselice et al. 2003). The morphology has been measured in the filter corresponding to rest-frame  $B$ -band. Sources detected in the FUV are plotted as filled circles. The dotted line indicates the minimum asymmetry for typical mergers.

This figure "f3.jpg" is available in "jpg" format from:

<http://arXiv.org/ps/astro-ph/0606244v1>



This figure "f10.jpg" is available in "jpg" format from:

<http://arXiv.org/ps/astro-ph/0606244v1>